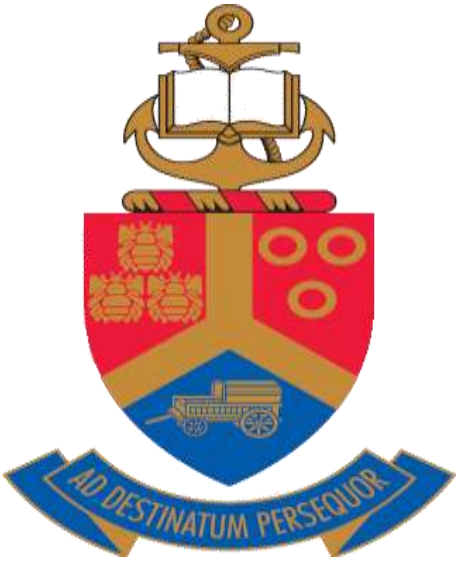

Experimental characterisation and statistical analysis of microstructure, porosity and mechanical properties for Ti6Al4V produced by high laser power powder bed fusion

Parmela Mana Madungandaba

Student number: 12373606

Supervisor: Prof. PGH Pistorius

Co Supervisor: Dr. H Moller

Submitted in partial fullfilment of the requirements for the degree

Master of Science Metallurgy

In the Faculty of Engineering, the Built Environment and Information Technology

University of Pretoria, Pretoria

DECLARATION OF ORIGINALITY

Declaration

1. I understand what plagiarism is and am aware of the University's policy in this regard.

2. I declare that this dissertation is my own original work. Where other people's work has been used (either from a printed source, Internet or any other source), this has been properly acknowledged and referenced in accordance with departmental requirements.

3. I have not used work previously produced by another student or any other person to hand in as my own.

4. I have not allowed, and will not allow, anyone to copy my work with the intention of passing it off as his or her own work.

DATE: 24 July 2019

ACKNOWLEDGEMENTS

Firstly, I would like to express my sincere gratitude to the Council for Scientific and Industrial Research (CSIR) National Laser Centre for the support provided throughout the project. Funding support by the Department of Science and Technology (DST) is acknowledged.

I would also like to thank all the colleagues and the experts at the National Laser Centre who participated in ensuring that the project was a success. Without their passionate participation and input, this work would not have been successfully completed.

I would also like to acknowledge Prof. Pieter Pistorius (University of Pretoria) and Dr Hein Moller (CSIR, NLC) for their guidance, support and numerous comments on this thesis. I am gratefully indebted to their support throughout this project.

Finally, I would also like to thank my family for providing me with continuous encouragement and support throughout the process of researching and writing this thesis. This work would not have been possible without their support.

ABSTRACT

Laser-powder bed fusion (L-PBF) processing finds its application in various metal forming industries such as aerospace, automotive and medical industries. Ti6Al4V alloy is widely used in aerospace applications. The main interest of studies on additive manufacturing of Ti6Al4V is to investigate the material properties (strength, toughness and corrosion resistance) with regards to applications in the aerospace industry. The L-PBF process allows great flexibility with regards to process control and process design, and therefore control over microstructure and properties.

The aim of the project was to study the effect of process parameters (laser power, scanning speed, hatch spacing, spot size and energy density) on Ti6Al4V microstructure and hardness of samples produced by L-PBF processing. The main objective was to analyse, and statistically predict part properties based on selected process parameters in order to enhance process understanding. The equipment that was used to manufacture the samples is a prototype powder bed fusion setup, with an Ytterbium laser system housed in a LENS (laser engineering net shaping) chamber. Experiments were carried out using a laser power of 1 to 3 kW, 2 to 4 m/s scanning speed, 0.10 to 0.24 mm hatch spacing, 250 to 450 µm spot size, and laser energy density of 33 to 200 J/mm^3.

Porosity analysis was conducted using the OHAUS Explore® balance precision weighing equipment. Optical microscope (OM) and EBSD analysis scanning electron microscope (SEM) was used to analyse microstructures of the samples.
Porosity was found to be a function of laser power, scanning speed, hatch spacing and energy density. Linear regression relationships were developed to predict porosity of Ti6Al4V under the set of parameters used in the study. The lowest level of fraction porosity obtained from the built parts was 0.6% (2 kW laser power, 2 m/s scanning speed, 0.24 µm hatch spacing and 450 µm spot size). The amount of porosity varied with laser power. A higher laser power resulted in increased micro round porosity.

A microstructure of acicular α martensite within columnar prior β grains was obtained for all energy density values used. Changes in process parameters used in the project scope were found to have a significant effect on the microstructure and not so much on the hardness range. However, through electron backscatter diffraction analysis a change in β content of (0.2 to 5.5%) was found with increasing energy densities, whilst content decreased with increasing energy densities. The hardness was between 326 and 418 HV (300 g).

LIST OF ACRONYMS

- AM- Additive Manufacturing
- DED- directed energy deposition
- L-PBF- Laser Powder Bed Fusion
- LENS- Laser Engineered Net Shaping
- FOD- Focal Offset Distance
- OM- Optical Microscope
- EBSD- Electron backscatter diffraction
- SEM- Scanning Electron Microscope

CONTENTS

TABLE OF FIGURES

LIST OF TABLES

1. INTRODUCTION

1.1 Background and motivation

There are various additive manufacturing (AM) processes available including laser-powder bed fusion (L-PBF), directed energy deposition (DED), sheet lamination, material extrusion, material jetting, binder jetting and VAT photopolymerization. This current study was focused on the laser-powder bed fusion (L-PBF) process, applied to a titanium alloy, Ti6Al4V, widely used in aerospace parts due to its combination of strength, toughness and corrosion resistant properties. L-PBF is an additive manufacturing technique that allows net shape fabrication of functional metal components. The process is defined as an additive manufacturing process in which thermal energy selectively fuses regions of a powder bed (ASTM52900-15, 2015). L-PBF processing finds its application in various metal forming industries such as aerospace, automotive and medical industries. The L-PBF process allows design freedom and reduces lead time for production. With regard to process control and process design, additive manufacturing PBF processing of Ti6Al4V requires a broader understanding of the solidification rates, thermal gradients and transformation products (microstructure and properties). Ti6Al4V undergoes epitaxial solidification, there-by forming large columnar prior-beta grains filled with alpha laths. The grain size and morphology of the solid are controlled by the nucleation and growth rate characteristics, cooling rate of the alloy and thermal conditions during solidification (Kobryn & Semiatin 2001, p.41). A diffusionless transformation, that is, the formation of non-equilibrium martensite is possible in Ti6Al4V, at high cooling rates. The columnar grain structure produces anisotropic mechanical properties which are non-desirable in applications requiring a combination of tensile strength and ductility, but are beneficial to creep resistant materials (Vilaro et al. 2011). 'Anisotropy is referred to as a directionality phenomenon, whereby properties of a material such as tensile strength vary depending on the direction along which they are measured' (Hutchinson 2015, p.1393). It is therefore preferable that the grain structure be engineered according to the requirements of the application (Easton et al. 2015). Heat treatment is applied in some cases for L-PBF produced parts to reduce residual stresses. During heat treatment above the beta transus temperature the alpha+beta structure completely transforms to beta. The beta that transforms on initial cooling to room temperature is metastable. The microstructures are dependent on the alloy chemistry, prior work, heat treatment temperature and cooling rate. Coarse and fine acicular structures can be produced but equiaxed structures are also possible (Donachie 2000, p.21).

The focus of this present study in L-PBF processing of Ti6Al4V was on the effect of process parameters (laser power, scan speed, hatch spacing and spot size) on porosity, microstructural evolution (in terms of the columnar prior-beta grain size and alpha grain size) and mechanical properties (as quantified using hardness measurements). The laser energy input during fabrication

can be best represented by laser energy density which is increased by increasing the laser power or decreasing the scanning speed, hatch spacing, and layer thickness (Zhang et al. 2016). These variables are known to govern the temperature gradient and cooling rate of the melt pool which in turn decides the morphology of the grains (Shukla & Verma, 2014). By varying the main process parameters, the temperature profile in the melt pool can be varied, which will change how the metal crystals nucleate and grow and finally allow control of microstructure and mechanical properties, with the limitation that the chosen parameters must still be able to produce a component with less than 0.2% porosity.

1.2 Aim and objectives of the investigation

1.2.1 Aim of the research

The aim of this project was to investigate the effect of process parameters during L-PBF processing of Ti6Al4V alloy, and develop empirical equations linking part properties with process parameters. Specifically, the effect of high (1 to 3 kW) laser power, spot size, scanning speed and energy density on microstructure, porosity and mechanical properties of the alloy was considered.

1.2.2 Objectives of the research

- Manufacture 10 x10 x 10 mm^3 cube samples using a prototype L-PBF powder bed fusion setup, utilising varied process parameters namely, laser power, scanning speed, spot size, laser energy density at a constant layer thickness of 50µm, by depositing gas atomized Ti6Al4V powder on a Ti6Al4V substrate.
- Carry out a microstructural, porosity investigation of the resultant samples, using optical microscopy, density measurement equipment and scanning electron microscopy (electron backscatter diffraction microstructural characterisation technique).
- To measure the Vickers hardness of the resultant samples.
- Analyse, and develop empirical equations linking part properties based on selected process parameters.

1.3 Significance of the research

Most research work available on L-PBF of titanium alloys focused on the influence of process parameters on the microstructure and mechanical properties. It has clearly been established that the processing parameters play a major role in the control and transformation of the microstructure and grain growth control during solidification. This particular research was focused mainly on determining the effect of process parameters on porosity, grain size of the large columnar prior-beta and alpha grains and mechanical properties. A unique aspect of this project was that a combination of high (1 to 3 kW) laser power and high speed was applied during L-PBF layer manufacturing of Ti6Al4V as opposed to previously published work, that used L-PBF with a laser

power ranging from 260 to 1000 W (Kobryn, 2001, Thijs et al. 2010 & Wu et al. 2004). The study of the PBF process capability to allow high laser power, high speed and high energy density studies contributes to the competitiveness/advancement of additive manufacturing in (building high complex parts-free of defects without using conventional casting and metal forming processes, increasing system productivity for industrial productions). The major benefits of using high laser power and high speed in additive manufacturing PBF technology among others are; energy saving, less material consumption, and efficient production. This technology innovation has the power to lead and improve supply, with long-term gains in efficiency and productivity. The study contributes to the country's current key economic concerns and is in-line with opportunities presented by the fourth Industrial Revolution. The fourth industrial revolution is said to bring about smart manufacturing techniques and technologies that will change products, processes and supply chains. This technology will enable manufacturers to maintain their competitive edge in a rapidly changing world, and respond to flexibly and quickly to customers' requirements (EEF, 2016).

1.4 Limitations and scope of investigation.

The laser system setup used initially presented a challenge with regard to changing the spot size, due to the fact that the laser fibre unit was a multi-mode system. Changing the spot size while using a multi-mode fibre caused a complete change of the sample profile during the process. Hence the first trial samples were processed at a constant spot size of 250 μm and a laser power of 1 kW, rather than the planned 1 to 3 kW power. The energy density calculated as laser power/ (speed x hatch spacing x layer thickness) during the first set of trials was in the order of 33 to 67 J/mm^3. Processing at high power and low speed, resulted in high amounts of melt pool splattering, posing a risk of damaging the optics. The second set of trials used an increased spot size 450 μm and power of 2 to 3 kW. The scanning speed was 2 to 4 m/s. During the second set of trials, no high melt-pool splatter problems were experienced. The energy density during the second trial was in the order of 42 to 200 J/mm^3.

2. LITERATURE REVIEW

2.1 Additive manufacturing processing

Additive manufacturing (AM) is a process in which a product is built layer-by-layer. The key feature of the process lies in completely joining successive layers. The process allows building of almost all types of materials (Kumar & Pityana, 2010). There are several AM classification systems available in literature (Wong & Hernandez, 2012 & ASTM52900-15, 2015). In this current study, the ASTM F42 was used (ASTM52900-15, 2015). AM manufacturing technology builds physical 3D geometries by successive addition of material. Addition of material means that units of material feedstock are brought together and joined by (e.g. fusion / bonding), most commonly layer by layer to build a part. The product fundamental properties are determined by: 1.The type of material (e.g. polymer, ceramic, metal or composite), 2. Principle applied for fusion or bonding (melting, curing, or sintering), 3. Feedstock that is used for adding material (liquid, powder, suspension, filament, sheet etc.) and 4. How the material is brought together i.e. machine architecture. The process of successively adding material to build a part makes the properties of the material highly dependent on the machine type and the process parameters. Depending on the process, parts may acquire the basic geometry and fundamental properties of the intended material in a single step process, or acquire the geometry in a primary process step, and then acquire the fundamental properties of the intended material for example; metallic properties for an intended metallic part in a secondary process step, Figure 1. The single and multiple step processes may require one or more additional post-processing operations such as heat treatments, finishing and machining (ASTM52900-15, 2015).

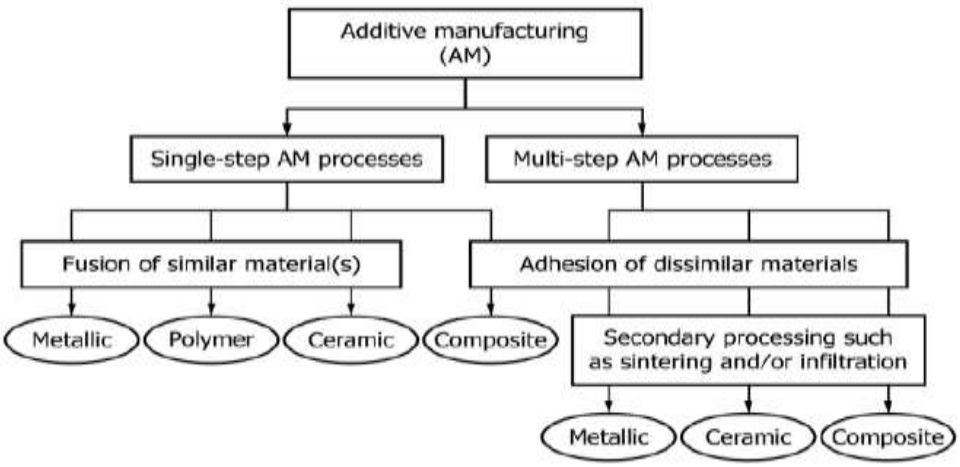

Figure 1: Single step and Multiple step AM process principles (ASTM52900-15 2015, p. 6, Figure A1.1)

L-PBF processing is an additive manufacturing technique that is successfully used in the manufacture of various metallic parts. Laser powder bed fusion deposition allows the use of a laser beam passed

over a powder bed to fuse a selected area, whilst the excess powder is re-usable. The laser beam path is derived from a 3d computer-aided design (CAD) model of the component. The platform supporting the bed of powder is then lowered by a precise distance and a further layer of powder is spread onto the bed. The cycle is repeated until shape is created in three dimensions. Thermal energy is used to selectively fuse the areas of a layer of powder using a laser. The energy source then traces the geometry of an individual layer onto the top surface of the powder bed, whilst the energy from the beam spot is absorbed by the exposed powder causing powder to melt and form a melt pool that quickly solidifies. After one layer is completed the build platform is lowered by the layer thickness and a new layer of powder from the dispenser container is swept over the build platform filling the resulting gap and allowing a new layer to be built (Mani et al. 2015). See Figure 2 for a typical L-PBF setup.

The AM (L-PBF) technology is of interest in this study because it forms part of a much larger project called Aeroswift (CSIR, NLC in collaboration with Aerosud), which is a project focused mainly on additive manufacturing of aerospace parts. The role of this particular project is to investigate or study the microstructure and mechanical properties of Ti6Al4V (powder metal) produced by AM (L-PBF) processing using a laser fibre unit with high laser power (up to 3 kW).

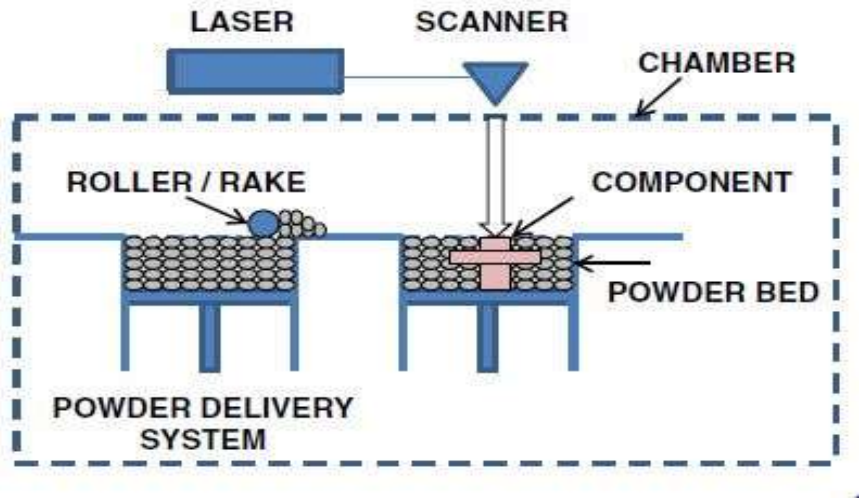

Figure 2: Schematic Setup of L-PBF Building Platform (Frazier 2014, p. 1919, Figure 1)

2.2 The effect of process parameters during additive manufacturing by means of powder bed fusion (L-PBF) processing

The process is influenced by the energy input of the laser which is best represented as laser energy density. The laser energy density E (J/mm^3) is defined as the energy supplied by the laser beam in unit volume as shown in equation 1 (Thijs et al. 2010 & Zhang et al. 2016).

$$\mathrm{E} = \frac{P}{vht} \tag{1}$$

Where (P) is the laser power (W), (v) is the scanning speed (mm/s), (h) is the hatching spacing (mm), and t is the layer thickness. Generally these parameters have a complicated mutual effect during the laser melting process when all of the parameters are varied in an experiment. Better tailoring and understanding of process parameters are of paramount importance in obtaining a better control of the resultant component. The most critical parameters are laser power, laser spot size, hatch spacing, the scanning parameters; laser scanning speed, the scanning strategy, and the material properties such as the surface tension and the thermal conductivity of the alloy.

During AM, the melt pool is produced by a sharply focused heat source laser (in a form of laser power) at a certain scanning speed. Solidification occurs rapidly in a small localized volume. The resulting microstructures are affected by repetitive thermal cycling. The thermal effects are due to factors such as that L-PBF process involves the deposition of a cold powder on a cold substrate/base plate (in some instances the substrate/base plate is pre-heated to limit thermal effects). The deposition of powder onto a cold substrate, and melting the powder at high energy densities results in rapid solidification and high cooling rates which leads to the presence of non-equilibrium phases. The melt pool solidification will determine the amount of porosity and surface roughness (Antonysamy, 2012). Bourell et al. (2017) experimentally investigated the effects of hatch spacing and layer thickness on porosity, and found that both parameters affect part density but did not report a quantitative correlation. Tang et al. (2018) investigated 10 x 10 x 10 mm^3 cubic parts which were built using a combination of parameters, and the averaged density was used in the analysis. The relative densities for the companion cubes with identical parameters, typically differed by less than 0.5% indicating the consistency of the fabrication process. Tang et al. (2017) also presented a geometry based simulation used as a tool to predict porosity caused by insufficient overlap of melt pools (lack of fusion) in L-PBF. The inputs in the simulations were hatch spacing, layer thickness and melt pool cross-sectional area. The melt pool areas used in the simulations were from experiments or estimated with the analytical Rosenthal equations. In these simulations, it was assumed that only insufficient melt-pool overlap causes lack-of-fusion porosity and that powder flow is not limiting. The simulations predicted both the process conditions beyond which porosity started to increase and rates of porosity increase (with higher beam speed, hatch spacing, or layer

thickness). Change in porosity was observed in parts built at the same energy density. It was also noted that energy density increase does not necessarily improve part density, and that maintaining a constant energy density (while changing other processing conditions) may result in varying porosity. Both the measurements and the simulations demonstrated that maintaining the same energy density does not guarantee a constant porosity.

The grain size and grain morphology that result from solidification of Ti6Al4V are primarily controlled by the thermal gradients and cooling rate of the melt pool, whereas the transformed microstructure is primarily controlled by the post-solidification cooling rate (Kobryn & Semiatin, 2001).

2.2.1 The combined effect of laser power and scanning speed

The L-PBF process is generally characterised by high scanning speeds and high temperature changes leading to high cooling rates and non-equilibrium microstructures. The cooling rates are affected by the laser energy. Lower laser power and higher scanning speed gives lower heat input and hence a higher cooling rate (Pinkerton et al. 2006). High energy density is induced by slower scanning speed leading to high temperature melt pools which in turn decreases the surface tension and improve the wettability of the liquid metal. The slower scanning speed keeps the metal in liquid phase for a longer period and ensures sufficient fluidity to flow between dendrites and backfill the dendrite shrinkages (Zhang et al. 2016). According to Pinkerton et al. (2006) when laser power is increased and scanning speed decreased a higher heat input occurs and more of the substrate is heated so cooling rates are reduced.

2.2.2 Effect of spot size and powder interaction time

The laser spot size is controlled by the focal offset distance (FOD) for a given laser beam source and optic lens. In laser manufacturing applications the focal offset distance (FOD) is defined as a critical parameter that controls the amount of energy delivered to the work piece (Chow et al. 2013). The FOD is also known to affect the local applied energy within the laser beam spot ($E' = 4P/\pi v D^2$, where E' is the local applied energy, P is the laser power, v is the scanning speed and D is the laser spot size of a circular beam). An increase in FOD increases the laser spot size D, which reduces the local applied energy E' but increases the powder interaction time.

It is also important to note that the variation in process parameters has an effect on the density of the built sample. A certain amount of laser energy intensity and powder interaction time is required to ensure a fully dense structure is produced. Louw (2016) investigated the effect of process parameters on the porosity of 3kW laser L-PBF Ti6Al4V processed parts. The measured percentage porosity of the built parts was observed to vary as a function of the build rate. An increase in spot size with higher build rates produced less porosity as opposed to lower spot size and lower build rate.

2.3 The metallurgy of titanium alloys

Titanium and its alloys find a widespread application in the chemical, aerospace, marine and medical fields, due to low density, excellent corrosion resistance, and high strength to weight ratio. Ti6Al4V specifically is widely used in the aerospace industry. Ti6Al4V was used in the current study due to the involvement of Aerosud (a producer of aerospace parts) in the larger project.

2.3.1 Solidification behaviour of Ti6Al4V

The important variables that control the melt pool solidification behaviour are the growth rate, cooling rate, temperature gradient, melt pool shape, travel speed, undercooling, and alloy composition which will all control the final microstructure of a solidifying melt pool in welding and in AM (Antonysamy, 2012). The solidification behaviour controls the size and shape of grains in the microstructure, the extent of segregation, the extent of defects such as porosity and hot cracks and ultimately the properties of the component. It is thus important to understand the development of the solidification microstructure by considering the nucleation of solid phases, and the development of the solidification morphology. The influence of parameters such as temperature gradient, growth rate and undercooling must be taken into consideration.

Solidification rate

The solidification rate or growth rate (R) is the rate at which the solid/liquid interface in the melt pool advances. R is directly related to the travel speed of the heat source (v). The rate at which the solidification front moves has a significant effect on the scale of the solidification substructure, the growth undercooling and the solid redistribution during solidification. In a steady state condition, in welding or AM where the heat source is moving at constant speed (v), solidification growth must occur in such a way that it is able to keep pace with the travel speed of the heat source.

$$R = v\,Cos\theta \qquad (2)$$

Where θ is the angle between the surface normal n and the heat source travel direction. At the top surface (assuming that the solidification front is normal to the surface), the growth rate would vary from R = 0, when θ is = 90° along the fusion line to a maximum R = $v\,Cos\theta$ (travelling speed of heat source) when θ = 0° along the centre line of the melt track. The local average growth direction during solidification of a melt pool is approximately perpendicular to the solid-liquid interface and parallel to the maximum thermal gradient against the heat flux. However the growth rate is also influenced by the crystallography through specific preferred directions, known as easy growth directions. For Ti6Al4V hexagonal close packed systems the preferred directions are close packed <1120> directions. These directions can grow much faster than other directions during solidification of liquid metals. During welding of a polycrystalline material, a wide range of grain orientations are present. A grain selection process will thus take place in which grains whose easy growth directions are optimally aligned with

the solidification front normal will selectively outgrow less optimally aligned grains. This selection process occurs for planar, cellular and dendritic growth (Kurz et al. 2001).

Thermal gradient

The thermal gradient in the solid (G_S) and in the liquid (G_L) at the solid/liquid interface plays a significant role in determining the solidification substructure in the melt pool. It is quite difficult to measure the exact thermal gradient in welding or AM. For high energy density processes using electron beams, lasers, the thermal gradient is higher than low energy density processes. The heat flow in AM processes is directional, frequently resulting in columnar microstructures. Vilaro et al. (2011) reported large columnar grains 150 μm wide. Re-melting resulted in a strong texture as a result of epitaxial growth on columnar grains in the substrate. Generally, AM is a relatively rapid solidification process (Zhang et al. 2016). The combined effect of rapid solidification, directional cooling and phase transformation induced by repeated thermal cycles has a significant influence on the microstructures produced from the deposited layers. Solidification in L-PBF leads to two types of grain morphologies; columnar and equiaxed. After nucleation of crystals in an undercooled isothermal melt, growth is normally equiaxed, i.e. it proceeds equally in all directions. In this way, eutectic or dendritic morphologies form a polycrystalline solid with randomly orientated grains. During columnar growth the heat flows from the superheated melt into the cooler solid (temperature gradient $G > 0$). A transition from columnar to equiaxed growth takes place when nucleation of equiaxed grains occurs in the liquid ahead of the columnar zone (Kurz et al. 2001).

Columnar growth formation occurs when an increased growth velocity decreases the size of the solute diffusion field in front of the growing grain during solidification (Easton et al. 2015).

Kobryn & Semiatin, (2001) suggested the use of solidification maps, (see Figure 4) to predict the solidification microstructure of Ti6Al4V. The solidification map was constructed by measuring the two critical solidification parameters; thermal gradient G, and growth velocity R using equation 3 and 4.

$$R = dz/dt \tag{3}$$

$$G = dT/dz \tag{4}$$

Where R is the solidification velocity calculated based on distance dz moved by solidus isotherms over a certain amount of time dt, and G is the thermal gradient which can be obtained using temperature window dT between solidus and liquidus isotherms over a certain amount of distance.

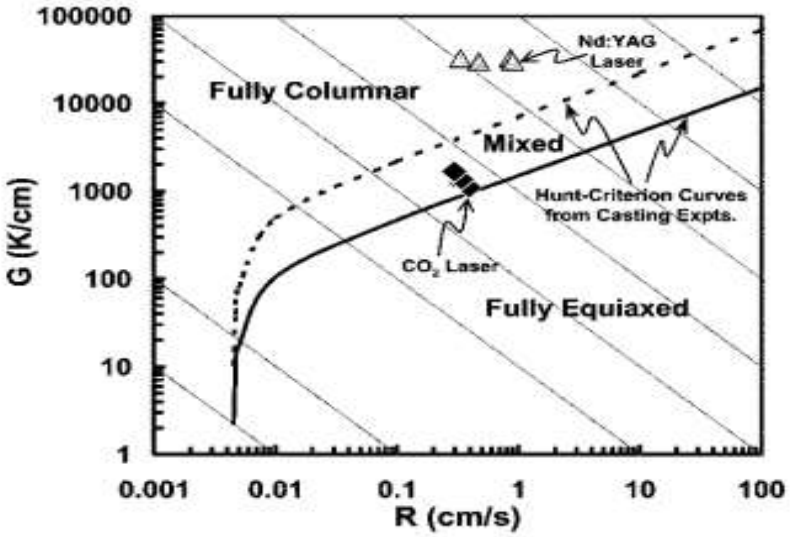

Figure 3: Solidification map of Ti6Al4V with simulated laser-glazed data taken at a constant cooling rate. Diagonal lines representing a constant cooling rate, (G.R in K/s) (Kobryn & Semaitin 2001, p. 335, Figure 4)

Cooling rates

The cooling rate plays an important role in determining the melt pool microstructural characteristics. Cooling rates in welding and AM can vary from 10^3-10^7 K/s depending on the process parameters (Vilaro et al. 2011 & Antonysamy, 2012). Solidification maps show the variation of the microstructure as a function of temperature gradient (G) and growth rate (R) as in Figure 3. Ti6Al4V is known to form large prior columnar beta grains during L-PBF. See Figure 4 for an illustration of the formation of columnar grains during laser metal deposition. These particular grains arise during solidification of the small melt pools generated by very high thermal gradients and cooling rate of high magnitude. This in turn leads to the development of very fine microstructures and a tendency toward exclusively columnar growth. Columnar grains tend to extend across deposited layers suggesting that the columnar crystals grow epitaxially from the substrate of previously deposited layers, the grains of which are partially re-melted and act as pre-nuclei (Pinkerton et al. 2006). Rapid cooling from L-PBF processing enhances the nucleation rate in the β grain boundaries thereby promoting the formation and growth of α platelets into the prior β grains. The length and width of the platelets are determined by the cooling rate. An increased cooling rate enhances the nucleation rate and slows diffusion (Pederson, 2002).

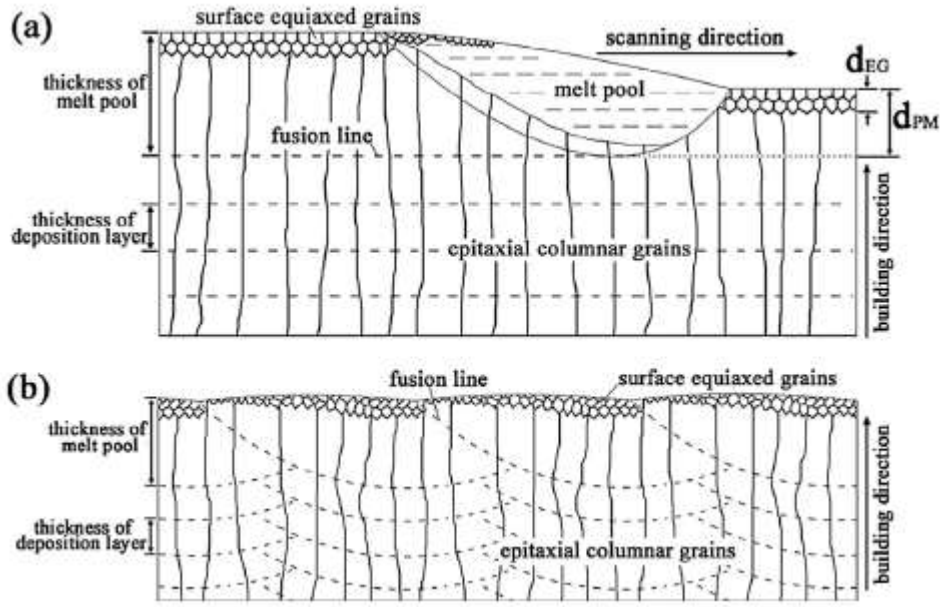

Figure 4: Schematic illustration for the formation of large columnar grains for titanium alloy components during the layer by layer laser melting deposition manufacturing process in longitudinal (a) and transverse (b) cross sections (Wang et al. 2015, p.511, Figure 14)

Wu et al. (2004) studied microstructures of laser deposited Ti6Al4V in direct laser fabrication. Under varied process parameters (laser power, scan speed, and powder feed rate), columnar grains dominate the solidification structure. With an increase in temperature gradient and growth rate, the columnar grains become shorter and they are gradually replaced by large equiaxed grains as depicted in Figure 5 (f), (d) and (e). An increase in scan speed resulted in a decrease in the size of alpha and beta laths in the basket weave microstructure. (Not shown in Figure 5, the authors also reported that) the highest scan speed produced a significant amount of porosity in the matrix and at the grain boundaries. Repeated thermal cycles have a possible complex set of effects, including microstructural banding.

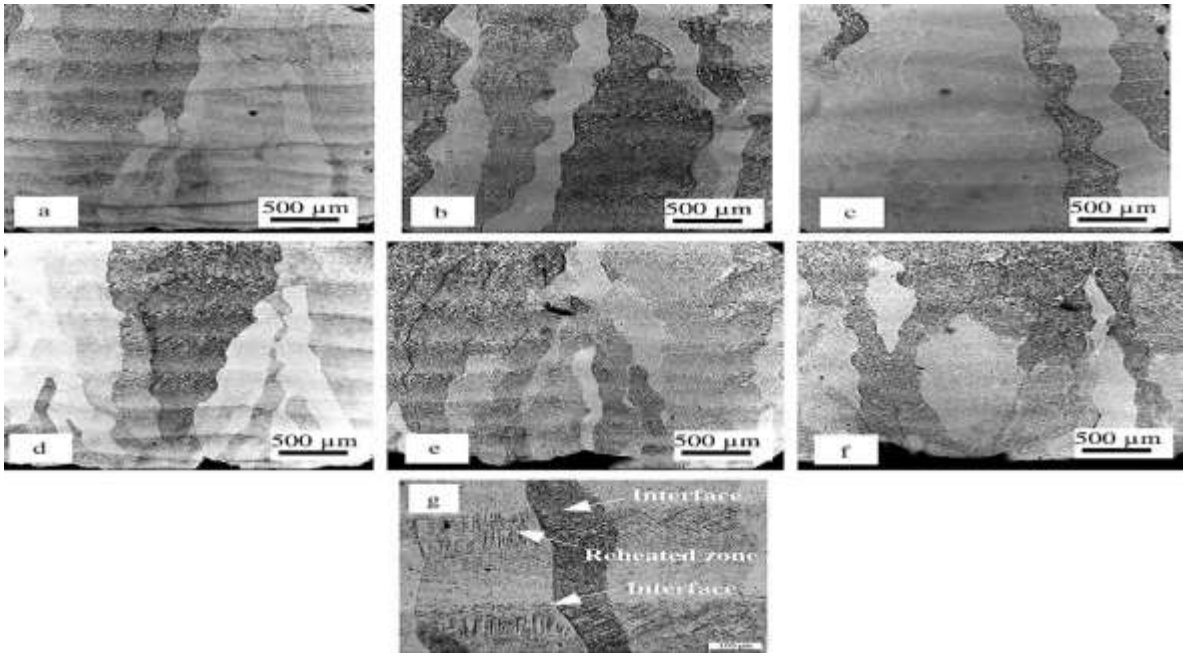

Figure 5: Optical morphologies of direct laser fabricated samples obtained: (a-c) at the bottom, centre and top locations, fabricated at 264W, scan speed of 300mm/min and powder feed rate of 12g/min and (d-f) at the bottom of the samples, fabricated at 300mm/min, 12g/min and at laser power of (d) 390; (e) 474, (f) 516 W and (g) showing columnar grains and layer bands which consist of coarse α and β laths in the heat affected zone below the interface (Wu et al. 2004, p. 139, Figure 1)

2.3.2 Solid state phase transformations during L-PBF of Ti6Al4V

At room temperature, titanium has a hexagonal close-packed crystal (hcp) structure, referred to as an alpha phase. Upon heating up to temperatures of up to 885ºC, pure titanium structure transforms to a body-centred cubic (BCC) crystal structure, referred to as a beta phase. Titanium alloys are therefore classified into four categories, namely: alpha alloys, near alpha alloys, alpha-beta alloys and beta alloys. The categories denote the general type of microstructure after processing (Donachie, 2000). Ti6Al4V is an alpha+beta alloy, as aluminium stabilises α phase, and vanadium stabilises β phase. The effect of alloying elements which are generally classified as alpha and beta stabilizers is stated as;

- Alpha stabilisers: elements such as aluminium, oxygen, nitrogen and carbon which raise the transformation temperature
- Beta stabilisers, such as vanadium, hydrogen which lowers the transformation temperature

The alloy composition completely transforms to beta upon heating but transforms back to alpha or/ plus retained transformed beta at lower temperature. For very slow cooling rates, from high up in the (α + β) region or above the transus temperature (995±20) °C the β phase transforms mainly to globular α (Wanhill et al. 2012).

Upon the high cooling rates from the β phase field the transformation to α occurs by displacive transformation to form a martensitic structure designated as α' (acicular plate-like martensite).

Increasing the cooling rate enhances α nucleation rate in the grain boundaries thereby enhancing the formation and growth of α platelets into the prior beta grains. The length and width of these platelets are determined by the cooling rate. A lower cooling rate may result in a lower fraction of martensite in the microstructure of Ti6Al4V (Xu et al. 2015). There are several types of martensite formed in titanium alloys depending on the cooling rate. The beta to martensite transition is responsible for an acicular (plate-like) structure in quenched and or quenched and aged titanium alloys. The morphology of the phases changes with prior treatment. The alpha phase present at the time of cooling can remain relatively globular (equiaxed), but the transformed beta (martensite or alpha) can be very acicular or elongated. The amount of equiaxed alpha and the coarseness and fineness of the transformed beta products affects the alloy properties. Intermetallic compounds and transient secondary phases also may be formed in the alloy system with microstructural variants of the traditional beta and alpha phases (Donachie, 2000).

In summary, as-fabricated L-PBF Ti6Al4V is known to have high strength and low ductility due to high thermal gradients and high cooling rates associated with the process. These properties are as a result of high cooling rates and rapid solidification referred to as epitaxial solidification. Through epitaxial solidification large columnar grains tend to grow and dominate the structure, which brings about anisotropic behaviour. Diffusionless transformation then leads to non-equilibrium phases such as martensite in the microstructure which is responsible for low ductility and high strength. However, through proper selection of L-PBF processing variables it is possible to transform the non-equilibrium acicular α' martensite into near-equilibrium lamellar (α + β) without triggering noticeable coarsening (Xu et al. 2015).

2.3.3 Heat treatment of Ti6Al4V

Due to the high thermal stresses normally encountered with L-PBF produced parts, an annealing heat treatment may be done to reduce residual stresses and to improve properties such as ductility, machinability and dimensional stability. Solution treatment and aging is applied to increase strength, optimize properties such as fracture toughness, fatigue strength and high temperature creep resistance. (Antonysamy, 2012).

2.3.4 Mechanical properties of L-PBF processed Ti6Al4V

The typical mechanical properties of the as-fabricated L-PBF Ti6Al4V parts are a high yield stress, a high tensile strength (UTS) and a low ductility. Galarraga et al. (2016) reported AM as-built Vickers micro-hardness measurements values for both orientations (vertical and horizontal) to be similar averaging at 368HV, comparable to the values previously reported (Koike et al. 2011 & Murr et al. 2009).

In an investigation by Xu et al, L-PBF processed Ti6Al4V indicated a tendency to form the highest fracture strength among other AM techniques, and the ductility was the lowest (Xu et al. 2015). Mower & Long investigated the mechanical behaviour of Ti6Al4V produced by L-PBF. Tensile stress-strain behaviours on flat-plate specimens, stiffness and fatigue strength measurements were measured. Tensile deformation measurements were compared in engineering stress-strain plots showing the differences in yield behaviours between conventionally produced and layered AM materials, and the results were as follows (Mower & Long, 2016):

1. **Young's Modulus**: Specimens produced with direct metal laser sintering (DMLS) showed a slightly higher modulus (115 to 117 GPa) in the horizontal and vertical direction. Conventional Ti6Al4V in the annealed condition used as reference material had a Young's Modulus of 114 GPa.

2. **Ductility**: The conventional wrought Ti6Al4V exhibited a ductile behaviour, modest strain to fracture of approximately 0.1 whereas, horizontally grown DMLS Ti6Al4V specimens showed higher yield strength, but lower strain to fracture (about 0.05).

2.3.5 Porosity in additive manufacturing (L-PBF) processing of Ti6Al4V parts

Porosity is one of the major most common defects in Additive Manufacturing. The defect can be powder induced; processes induced or arise during solidification. In order to avoid porosity mechanisms, the process parameters must be properly set.

Pores that are formed due to the processing technique are known as process-induced-porosity. Processed-induced porosity forms when the applied energy is not sufficient enough for complete melting or can be due to the occurrence of spatter ejection. These pores are typically round and come in a variety of sizes, Figure 6. Different processing issues can create defects in the material some of which contribute to porosity.

When the applied power is too high, spatter ejection occurs in a process known as keyhole formation. The keyhole mode has been observed to produce a series of voids over the operating region in L-PBF processes (King et al. 2014). Spatter ejection may also lead to regions of porosity. Powder distribution on the processing surface includes particles larger in diameter than the layer thickness which upon melting are intended to consolidate into a layer of the correct height (Sames et al. 2016).

Shrinkage porosity sometimes occurs, due to the incomplete flow of metal from the desired melt region. With optimised process parameters, process-induced-porosity can be reduced to very low levels.

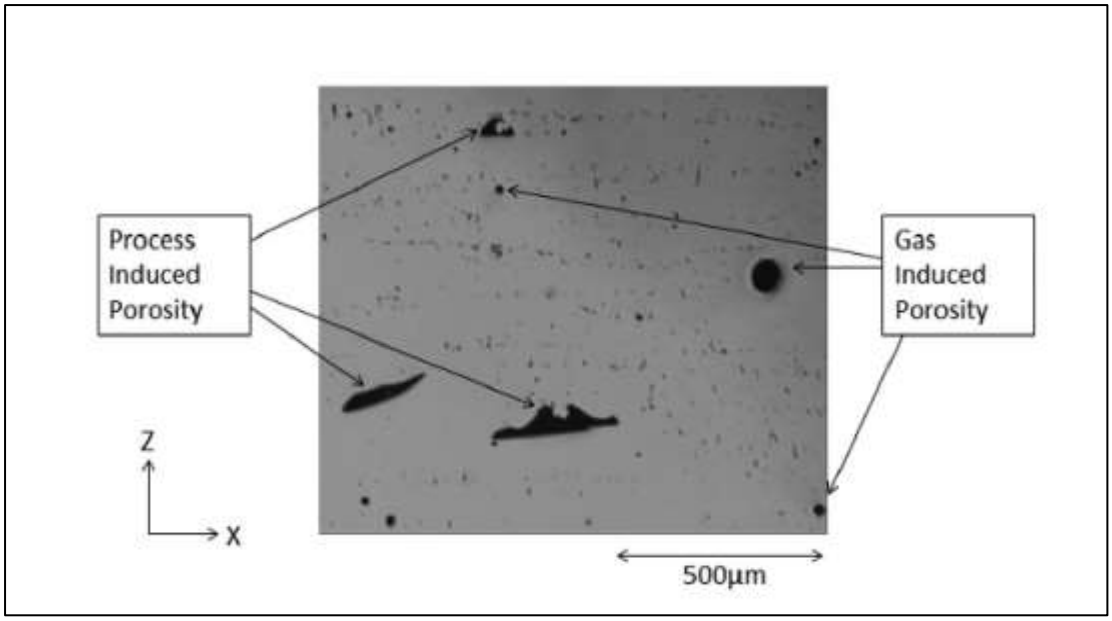

Figure 6: Light optical microscopy showing comparison of process- induced-porosity, lack of fusion porosity to, entrapped gas porosity transferred from the powder feed-stock (Sames et al 2016, p. 12, Figure 15)

Gong et al. (2013) investigated the effect of process parameters on defect regularity in Ti6Al4V parts fabricated by L-PBF. Similar to the current study, the process parameters (laser power and scanning speed) were varied. However a high range of laser power 1 to 3 kW and higher scanning speed 3 to 4 m/s was used in the current as opposed to the Gong et al. (2013) investigation. The results obtained from investigation, presented in Figure 8, demonstrated the influence of laser energy density, laser power and scanning speed on porosity. Samples that were fabricated when the scanning speed was less than 600 mm/s had higher energy density which resulted in increased porosity. When the laser power was reduced to 0.08 kW, a porosity free specimen was only available when the scanning speed was around 600 mm/s, as shown in Figure 7 (c). Lowering the scanning speed resulted in reduced amount of porosity as opposed to increasing the scanning speed. The porosity was dramatically increased when increasing the scanning speed. When the laser power was lowered to 0.04 kW, all specimens were assumed to contain defects even at a slow scanning speed. At 1200 mm/s, the porosity was even higher than 20%, as shown in Figure 7 (d).

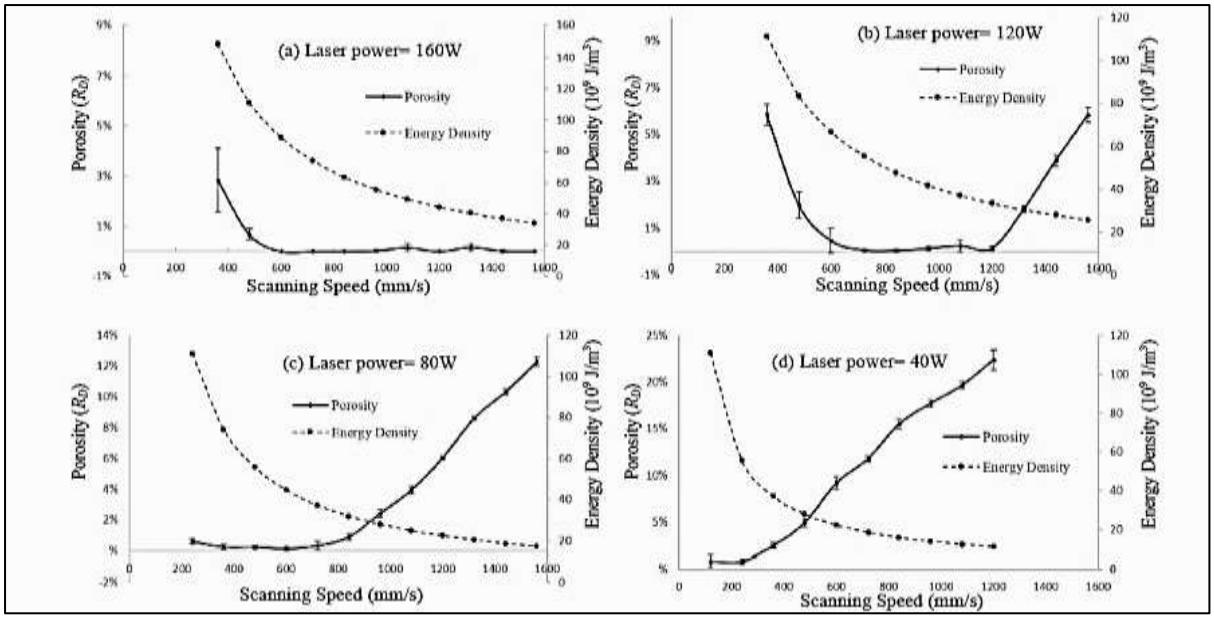

Figure 7: Porosity of L-PBF-Produced Ti-6Al-4V Specimen (Gong et al 2013, p. 428, Figure 5)

Kasperovich et al. (2016) presented a study conducted to investigate the correlation between process parameters and porosity formation. Similar to the current study, Ti6Al4V samples were L-PBF manufactured using varied process parameters (laser power, scanning speed, hatch spacing and energy density). The porosity was investigated by 2D and 3D methods aimed at identifying the mechanisms of void formation, morphology as well as volume fraction as a function of energy density. The porosity of each sample was characterised qualitatively and quantitatively by 2D image analysis of the metallographic longitudinal cross section (parallel to the L-PBF building direction) and three-dimensional by synchrotron tomography. Three parameter sets were selected for a detailed analysis of porosity i.e. excessive overheating $E_v > E_{opt}$ where E_{opt} = 117 J/mm^3, and insufficient energy $E_v > E_{opt}$, where E_{opt} was chosen considering the minimum porosity volume fraction as a function of scan velocity. The optimised energy E_{opt} obtained in the study was very close to optimum energy density of 120 J/mm^3 at hatch distance of 100 µm and layer thickness of 100 µm. It was noted that similar energy densities can be achieved by different combinations of parameter sets (laser power, scanning speed, hatch distance, scanning strategy and layer thickness). The major findings in the investigation with regards to porosity correlation to insufficient energy density, medium energy density and excessive energy density (58 J/mm^3, 117 J/mm^3 and 292 J/mm^3) are Figure 7 a – b were described as follows:

Insufficient energy density increases porosity, due to partially melted and entrapped powder particles that stick to an agglomerate on the outer edge of the solidified melt pool. This phenomenon is known as satellite formation (Tolochko, 2004). Satellite formation mainly occurs when powder particles are not given enough time or heat to penetrate the melt pool before melt pool solidification (Mumtaz & Hopkinson 2010). The pores appeared as elongated narrow crack-like voids orientated perpendicular to the building direction Figure 8 (a). These pores were as a result of binding faults (lack of fusion) owing

to incomplete melting of powders. At medium energy densities (117 J/mm^3), an almost pore-free microstructure was obtained, Figure 8 (b). Other researchers have attributed this phenomenon to the keyhole effect (Attar, 2014), (Pang, 2014) & (Rai, 2009). This is shown in Figure 8 (c). The keyhole effect is well known in the laser welding technology (Fabbro, 2019), and it creates a pore having a corner point and smooth surface wall. The laser ray imposes on the powder bed, some laser rays reflect out from the top surface of the powder zone, and some laser rays penetrate the powder bed. The laser ray penetrates the powder and mostly scatters at the bottom portion of the layer. Therefore, the bottom part of the powder layer gains a higher temperature than its upper part. The high temperature at the bottom part causes evaporation and thus forms a keyhole in the melt pool

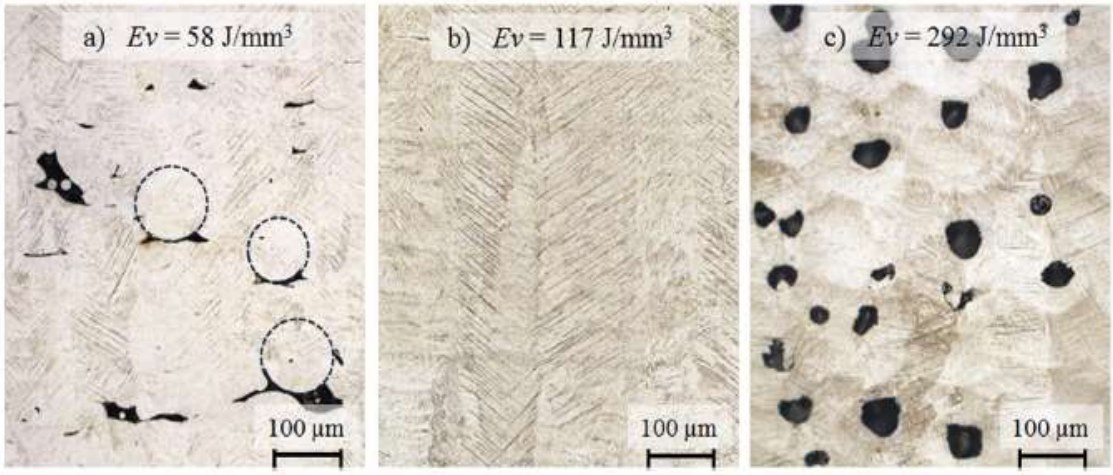

Figure 8: 2D Pore morphologies obtained by LOM after L-PBF processing with different energy densities: (a) Ev=58 J/mm^3 ≪Eopt, (b) Eopt=117 J/mm^3 and (c) Ev=292 J/mm^3≫Eopt. The pores arising from low energy density (a) were induced among other effects by the balling effect and by un-molten particles (dashed circles). Some showed satellite formation as evidenced by enclosed small spheres (c) (Kasperovich et al. 2016, p. 162, Figure 4)

2.4 Summary of published observations

Additive manufacturing laser-powder bed fusion processing is a process carried out with the use of a laser beam passed over a powder bed to melt and fuse a selected area. The key features of the process lie in the beam delivery of the thermal energy absorbed by the exposed powder, to deliver enough energy that can induce enough melting of the powder to form a melt pool, and consequently solidification.

The process is inherently characterised by high temperatures, high speed and rapid solidification. The critical process parameters are mainly the laser power, scanning speed, hatch spacing, layer thickness, laser spot size and the focal off-set distance. The key in fabricating a fully dense part lies in tailoring the best way possible combination of the critical process parameters hence the energy density that is

enough to melt the powder. One of the major findings in relation to the influence of laser energy density in Ti6Al4V AM processing was that at the lowest energy densities, porosity levels were very high due to less thermal energy to cause adequate melting. Excessive energy densities resulted in increased micro porosity. The microstructures obtained were that of typical L-PBF built parts i.e. martensitic microstructures that form due to rapid cooling from L-PBF processing whereby α nucleates in the β grain boundaries thereby promoting the formation and growth of α platelets into the prior β grains. The alpha platelets, alpha grain size and prior beta grains size were found to vary only slightly with the energy density.

3. EXPERIMENTAL METHOD

3.1 Methodology

The aim of the project was to study the effect of process parameters (laser power, scanning speed, hatch spacing, spot size and energy density) on Ti6Al4V microstructure and hardness of samples produced by L-PBF processing. The equipment that was used to manufacture the samples is a prototype powder bed fusion setup, with a Ytterbium Laser system housed in an Optomec 850-R LENS chamber. Experiments were carried out using a laser power of 1 to 3 kW, 2 to 4 m/s scanning speed, 0.10 to 0.24 mm hatch spacing and 250 to 450 µm spot size. Cube samples were manufactured by depositing gas atomized Ti6Al4V powder on a Ti6Al4V substrate in an argon purged environment where atmospheric oxygen content was kept at 200 ppm, see Figure 9. A equipment scraper was used to level the Ti6Al4V powder for every layer that was scanned with the laser beam path derived from a 3D CAD model of the cubes.

The experimental matrices were initially designed to build cubic parts at laser powers ranging from 1 to 5 kW. Due to operational issues, the highest power used was up to 3 kW, at varied increasing scanning speed from 2 to 4 m/s, spot size of 250 and 450 µm, at constant layer thickness of 0.05 mm. 10 x 10 x 10 mm cubic samples were manufactured at varied process parameters, and wire cut from the substrate before preparation for metallographic analysis.

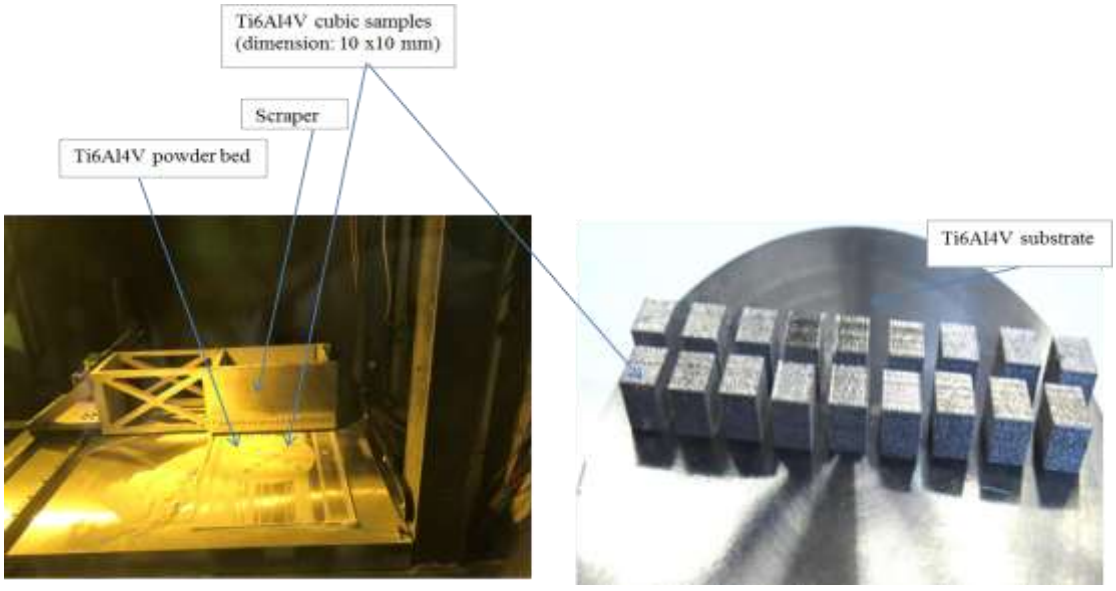

Figure 9: Powder bed sample manufacturing setup

3.1.1 Materials Used

Ti6Al4V base plate

The base plate used was a Ti6Al4V Grade 5 ASTM B265-10 base plate, supplied in the annealed condition.

Ti6Al4V gas atomised powder ASTM Grade 5 chemical composition

The chemical composition of the Ti6Al4V powder supplied by TLS Technik GmbH that was used in the project is set out in Table 2. Note the chemical composition with aluminium content of (5.6 - 6.7) % and vanadium content of (3.5-4.5) % typical of Ti6Al4V powder alloys used in L-PBF processes.

Table 1: Chemical composition of Ti6Al4V powder used in current study

	Aluminium Al %	Vanadium V %	Carbon C %	Oxygen O %	Nitrogen N %	Hydrogen H %	Titanium Ti %
ASTM	5.5 – 6.7	3.5 – 4.5	<0.1	<0.2	<0.05	<0.015	Balance

Ti6Al4V powder ASTM Grade 5 particle size characterisation

Ti6Al4V powder size characterization was conducted at (CSIR) Material Science and Manufacturing (MSM). The particle size analysis of the gas atomized Ti6Al4V powder was conducted using a Bluewave Microtrac laser diffraction particle size analyser. The ASTM B822 standard for particle size distribution of metal powders by light scattering was used (ASTM B822, 2017) Figure 10 presents the particle size distribution analysis results of the gas atomized Ti6Al4V powder that was used. The median particle size was 37 µm. The actual particle size met the requirement of Ti6Al4V powder alloys in L-PBF processing for aerospace parts. In contrast, the supplier claimed a particle size distribution of 38 to 50 µm maximum particle size. The powder flowability is a powder characteristic which can affect the particle distribution on the powder bed, which is itself affected by the powder particle size distribution. In L-PBF processing, good powder flowability is required to achieve uniform thickness of powder layers, which allows uniform laser energy absorption in the processing area (Liu et al. 2011). The SEM image analysis in Figure 11 revealed the powder particles as dominantly spherical rounded shapes with a few irregular and porous particles, indicating good flowability.

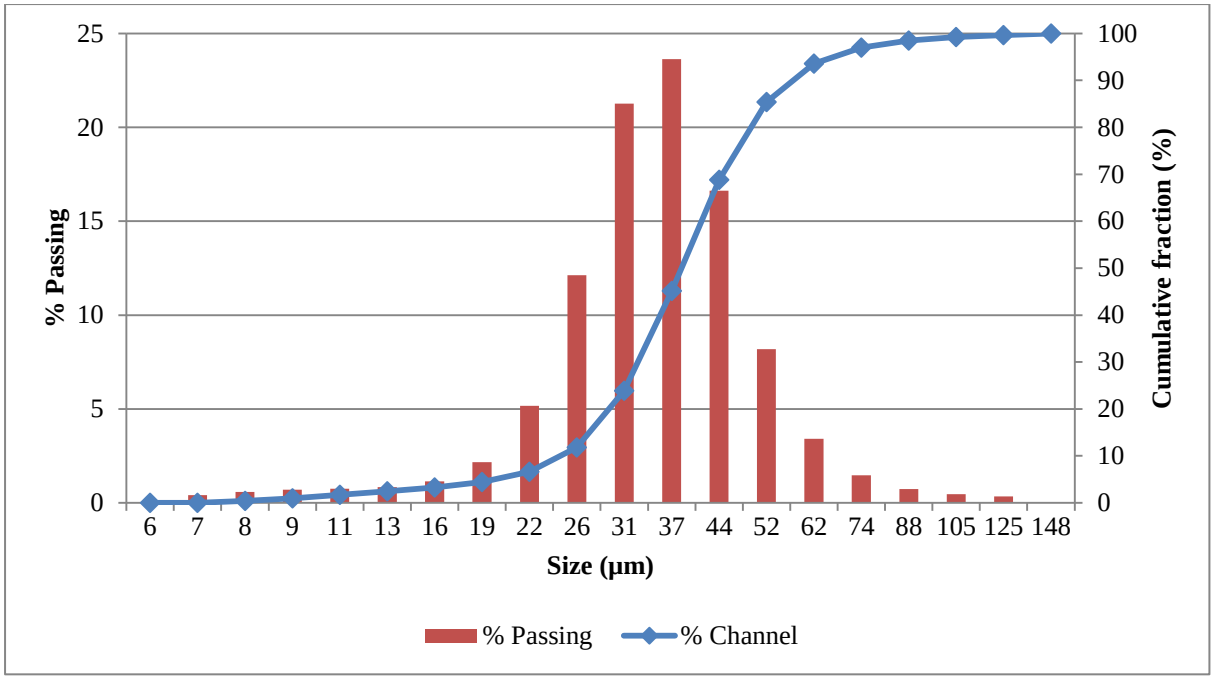

Figure 10: Powder particle size distribution analysis gas atomized Ti6Al4V

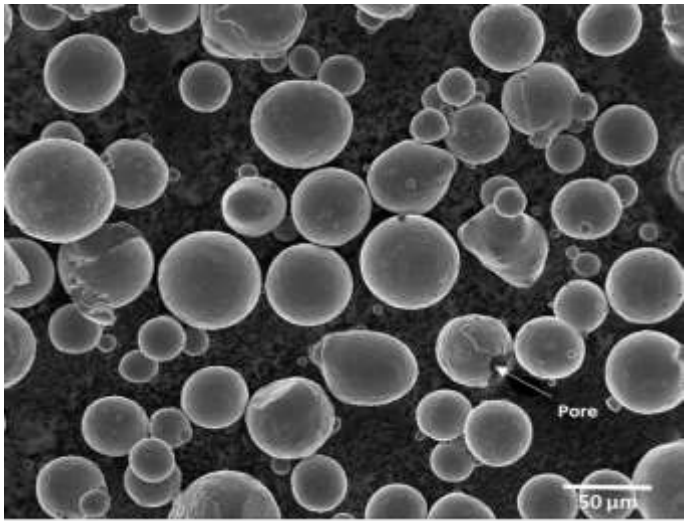

Figure 11: SEM image of the Ti6Al4V powder

3.1.2 Experimental matrix

Two sets of trials were conducted to manufacture the samples. In the first set of experiments, identified as Trial 1, samples were manufactured using a multimode laser with a constant spot size of 250 µm at low power (1 kW), increasing scanning speed 3, 3.5 and 4 m/s, and a hatch spacing of 0.10, 0.13 and 0.15 mm. The laser energy density was in the order of 33 to 67 J/mm^3. Attemps to build samples at higher powers of 2, 3, 4 & 5 kW were discontinued due to the level of uncontrollable melt pool splattering encountered posing a risk of damging the optics.

Trial 2 was done at different conditions to accommodate high laser power samples i.e (change of spot size, increased scanning speed, and increased energy density). Trial 2 samples were manufactured using a single mode laser with a constant bigger spot size of 450 µm at high power (2 to 3 kW), increased scanning speed (2 to 4 m/s) and energy density in the order of of 42 to 200 J/mm^3 . The bigger spot size made it possible to build samples at laser power of up to 3 kW maximum allowing adequate powder melting. As with trial 1, increasing the laser power to 4 kW resulted in melt pool splattering. Due to the splattering the laser power was limited to 3 kW. Table 2 outlines the experimental matrix.

Table 2: Experimental matrix: The layer thickness was 0.05 mm in all cases

	Sample ID	Power (kW)	Spot size (µm)	Scanning speed (m/s)	Hatch spacing (mm)	Energy density (J/mm^3)
Trial 1	**A1**	1	250	3	0.13	51
	A2	1	250	3.5	0.13	44
	A3	1	250	4	0.13	38
	A4	1	250	3	0.15	44
	A5	1	250	3.5	0.15	38
	A6	1	250	4	0.15	33
	A7	1	250	3	0.10	67
	A8	1	250	3.5	0.10	57
	A9	1	250	4	0.10	50
Trial 2	**B1**	2	450	4	0.24	42
	B2	2	450	2	0.24	83
	B3	2	450	4	0.10	100
	B4	2	450	2	0.10	200
	B5	3	450	4	0.24	62
	B6	3	450	4	0.10	150

The manufactured samples were wire cut from the base plate and metallographically prepared for microscorpic and porosity analysis using an optical microcope, scanning electron microscopeand Vickers micro hardness measurements on the front polished longitudinal side surface (building direction) of the sample (from bottom to the top of the build), see Figure 12.

3.2 Sample characterization and preparation

3.2.1 Cutting and mounting

The 10 x 10 x 10 mm^3 cube specimens were wire cut removed from the substrate, and mounted as is (10 x 10 x10 mm^3 cube) . The cubes were mounted as shown in Figure 12, exposing the built direction. The microstructures were therefore characterised in the exposed front surface of the cube, i.e from the bottom to top in the built direction, see Figure 12. Samples were mounted with a non-conductive black resin using a Struers Mounting Press-2 machine.

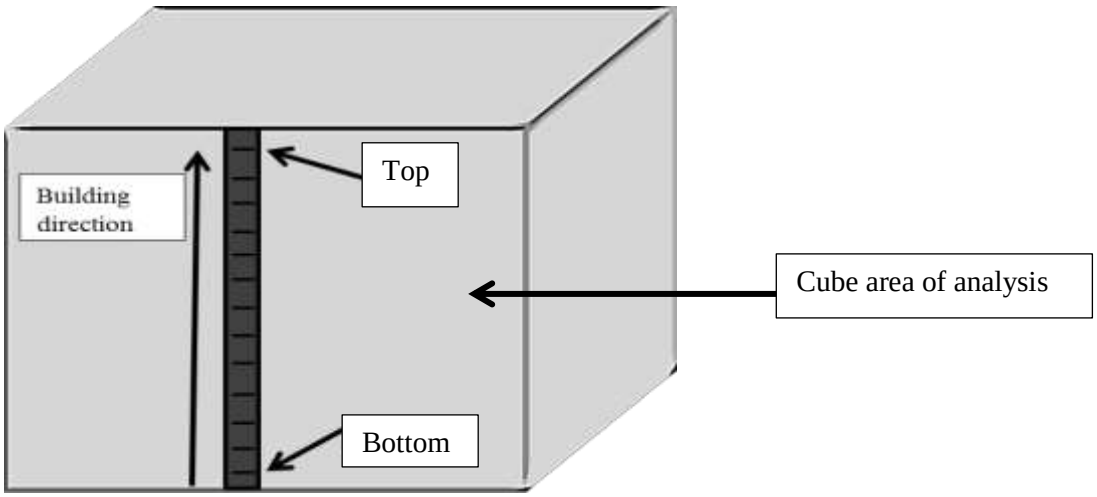

Figure 12: 3D Cube indicating the building direction during manufacturing and the position of metallographic samples

3.2.2 Grinding, polishing and etching

The first grinding step was conducted using a 320 silicon carbide grit paper. About 1mm was removed from the front surface of the 10 x 10 x 10 mm^3 cube, so that the rough surface would not affect subsequent characterisation (Figure 12). Further fine grinding was done using a 1200 grit silicon carbide paper, and final finer grinding using a 1400 grit paper. Final polishing was done using an automatic Struers polishing machine with an MD Chem polishing cloth/disc and an OP-S 0.04µm colloidal silica lubricant . Etching was done using Kroll's Reagent by immersing the polished specimens in the etchant for about 25 seconds (Technologies, 2006-2017). Kroll's reagent is the recommended etchant for titanium alloys, see chemical composition in Table 3.

Table 3: Kroll's reagent composition (Technologies, 2006-2017)

Etchant	Composition	Conc.
Kroll's Reagent	Distilled water	92 ml
	Nitric acid	6 ml
	Hydrofluoric acid	2 ml

3.2.3 Microstructural analysis

- **Optical microscopy analysis**

The etched samples were analysed on the optical microscope, microstructures taken at 5x and 10x magnification. The method of analysis was conducted to determine how the microstructure changed in the front built side first initial layers (bottom area), middle area to the top area of the sample. The porosity analysis was also conducted using the optical microscope with an image analysis programme (Stream Essentials) whereby the variation of the pores per sample was analysed in the 3 areas of the (10 x10 x10) mm^3 sample (bottom, middle and top). The dimension of the columnar prior beta grains in the horizontal direction was characterised by counting the number of intercepts on a horizontal line, consistent with the anticipated shape of the beta grain as shown in Figure 4.

- **Scanning electron microscope (SEM) analysis**

The samples were analysed on the Jeol JSM-6010 PLUS/LA model. Similar to the the optical metallographic analysis, the micrographs were taken on 3 areas of the (10x10 x 10) mm^3 sample (bottom, middle and top) in the front built side at 1000x magnification.

- **EBSD analysis**

Three representative samples were analysed. The samples were analysed for alpha grain size distribution, grains map orientation, alpha and beta using EBSD equipment with the following settings: accelerating voltage 25 kV, specimen tilt 70.00°, hit rate of 56.30%, and acquisition speed of 60.51 Hz.

3.2.4 Porosity analysis

The densities of the L-PBF built samples were measured using the OHAUS Explore® balance precision weighing equipment. The procedure followed was weighing the mass (g) of each of samples in air, and weighing the mass (g) of each of samples submerged in water. Once the necessary weights were determined, the equipment calculated the density of the samples in (g/cm^3). The measurements were repetaed 3 times per sample analysed density (g/cm^3) and averaged (Ave ρ_{sample}). For example, see sample 1 measurements in Table 4 and the rest of the samples in Table 16 in the appendix.

Table 4: Individual density measurements of sample A1

Mass (g)		**Density (g/cm3)**	**% Density**	**% Porosity**
Air	**Liquid**			
2.828	2.3201	4.3842	98.97	1.03
	2.3207	4.3929	99.16	0.84
	2.3206	4.3913	99.12	0.88
Average		4.3895	99.12	0.88
Range				0.84 – 1.03

See Table 4 for a sample calculation of the effect of the range in density measurements on the calculation of porosity. Figure 19 in Chapter 4 and Table 16 in the appendix shows the range in density measurements for all samples. The uncertainity in porosity was estimated to be significantly lower than the average porosity. The average range in porosity was 12% of the average porosity for the specific sample - higher range for low levels of porosity.

A standard reference average density of Ti6Al4V $\rho_{ref\ Ti6Al4V}$ = 4.4 g/cm^3 (Lampman, 1990) was substituted to equation 5 & 6 to determine the density (%) per sample. For the example in equation 5 a measured density of 4.39 g/cm^3 was used. The porosity was considered accurate as it showed significant correlation with the change in energy density (as will be demonstrated later in this document).

$$\%\ \text{Density} = (\text{Ave}\ \rho_{\text{sample}} / \rho_{\text{ref, Ti6Al4V}}) * 100 \quad (5)$$

$$= (4.39\ g/cm^3) / (4.43\ g/cm^3) * 100$$

$$\%\ \text{Porosity} = 100 - (\%\ \text{Density}) \quad (6)$$

$$= 100 - 99.12$$

$$= 0.88$$

3.2.5 Micro Vickers hardness test

Vickers hardness profiling were conducted on all the samples using an automated Vickers hardness machine, applied load of 300 g on the cross section of the sample from bottom to top in the build

direction. The hardness indentations were spaced at 1mm. An average hardness was calculated from all ten hardness measurements done on a specific sample.

4. RESULTS

In this section, the results of two trials are presented:

- Trial 1 used a constant laser power of 1 kW and a 250 µm spot size. The scanning speed was varied over three values (3, 3.5 and 4 m/s). At the same time, the hatch spacing was systematically varied at 0.10, 0.13 and 0.15 mm, resulting in nine separate trials.
- In Trial 2, the spot size was always 450 µm. The hatch spacing was either 0.10 or 0.24 mm, see Table 2 for details of all six samples produced in Trial 2.
- For all the trails, the layer thickness was 0.05 mm.

In this section, the energy density is quoted, calculated as noted in Section 2.2.

Energy density = E $= \frac{p}{vht}$

4.1 Trial 1 Results: Microstructure as a function of process parameters

The 1st trial samples manufactured using a constant layer thickness 0.05 mm, 250 µm spot size, 1 kW laser power, varied scanning speed and hatch spacing are presented in Figure 13, 14 & 15. An increase in the scanning speed resulted in higher porosity, if the other parameters were constant, for all the process settings used. The highest % fraction porosity observed was for samples manufactured at the highest scanning speed of 4 m/s.

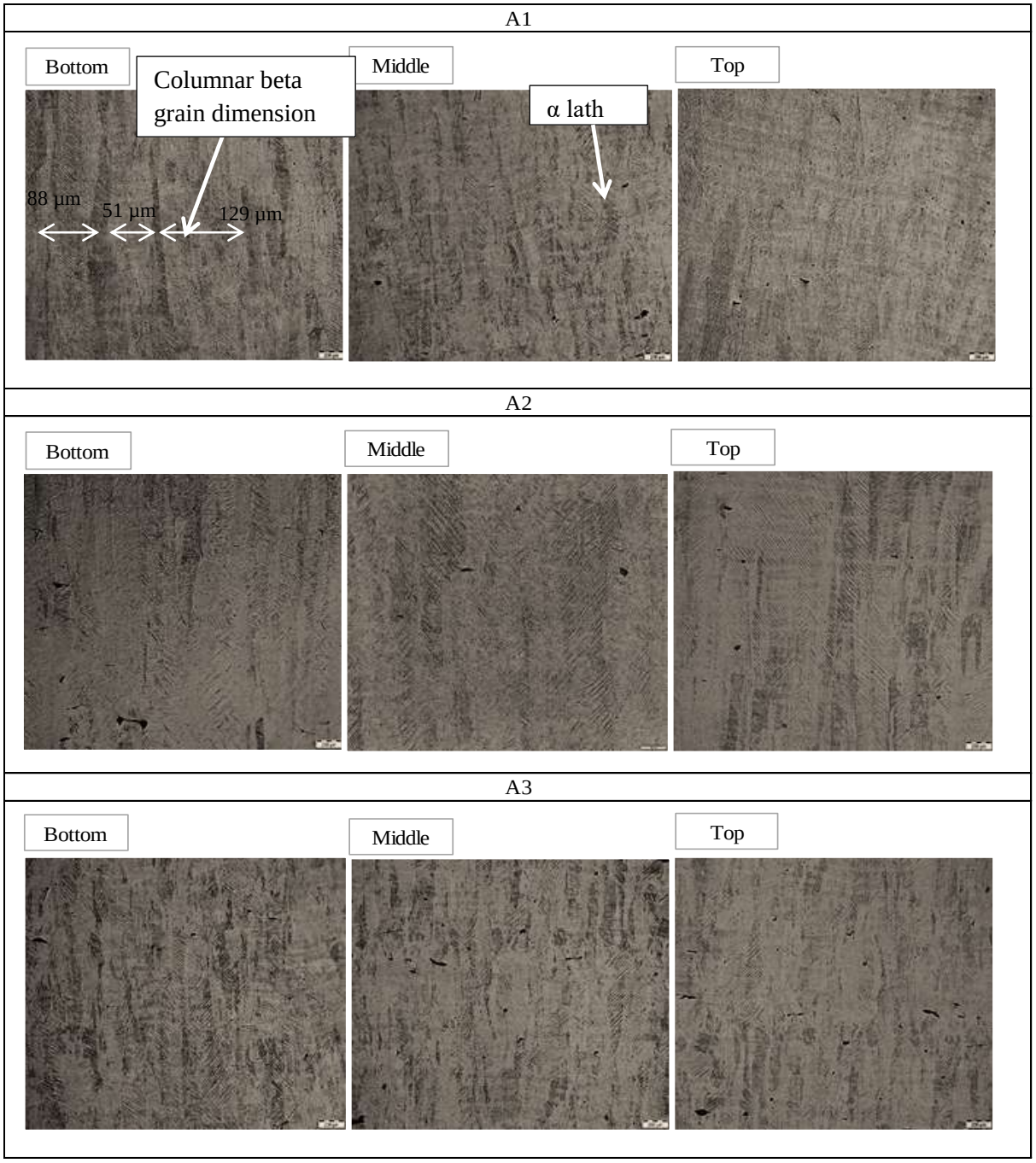

Figure 13: Microstructures of samples manufactured at 1 kW laser power, 3, 3.5 & 4 m/s scanning speed, 0.13 mm hatch spacing and decreasing energy density (51, 44 & 38) J/mm^3. The scale bar indicates 10x Magnification

The microstructures observed in Figure 13 is of acicular α martensite with alpha laths filling large columnar prior beta grain boundaries for all 3 samples (A1-A3). Sample A3 columnar prior beta grains appear shorter and more irregular than in A1 and A2. The presence of porosity also appears to be higher on sample A3 (produced at high scan speed and low energy density) than it is in sample A2 and A1.

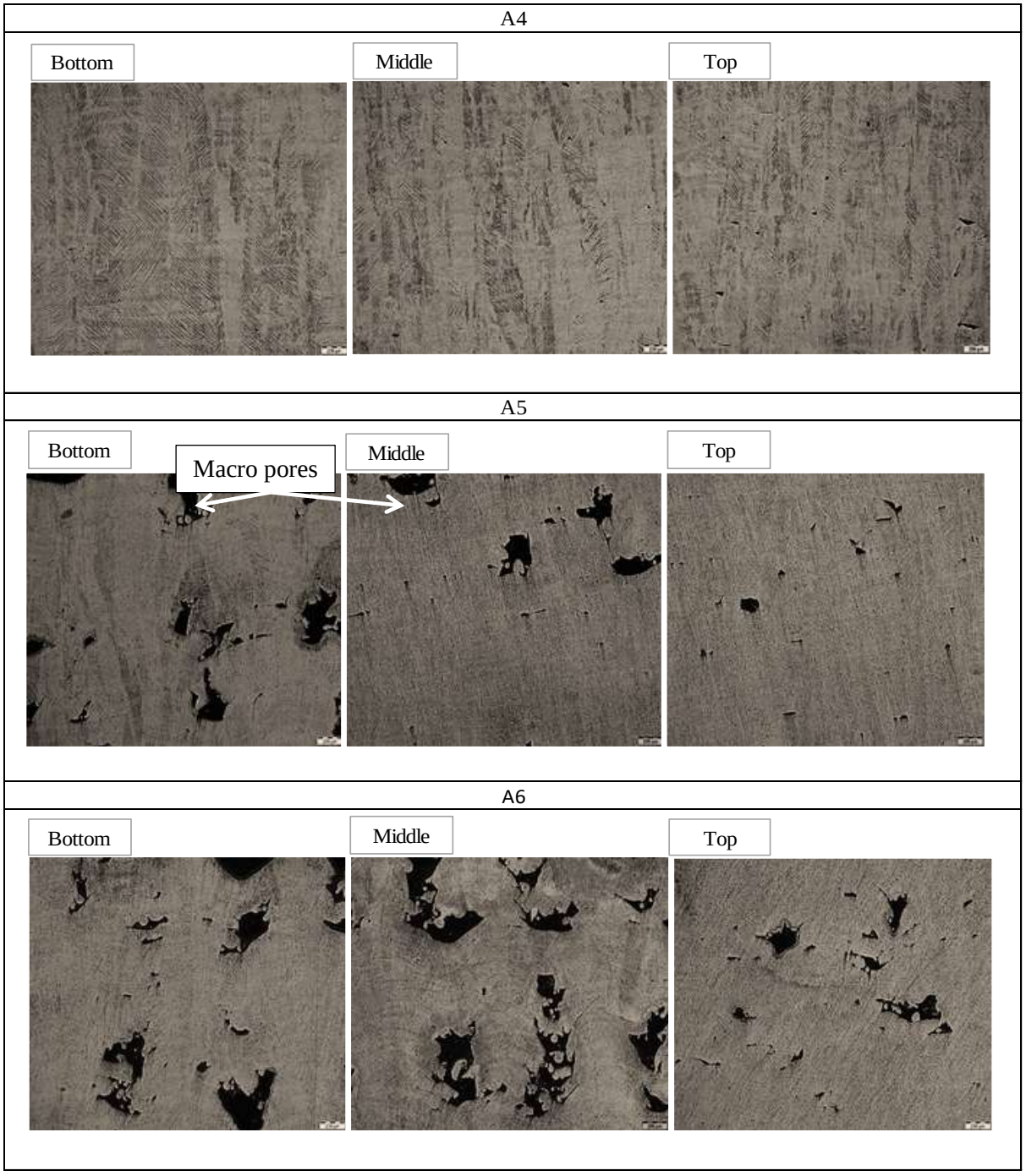

Figure 14: Microstructures of samples manufactured at 1 kW laser power, 3, 3.5 & 4 m/s scanning speed, 0.15 mm hatch spacing and decreasing energy density (44, 38 & 33) J/mm^3. The scale bar indicates 10x Magnification

Low laser energy density resulted in severe porosity in sample A5 and A6 – see Figure 14 samples. The microstructure was observed to be of acicular α martensite with α laths filling columnar prior β grains in all cases.

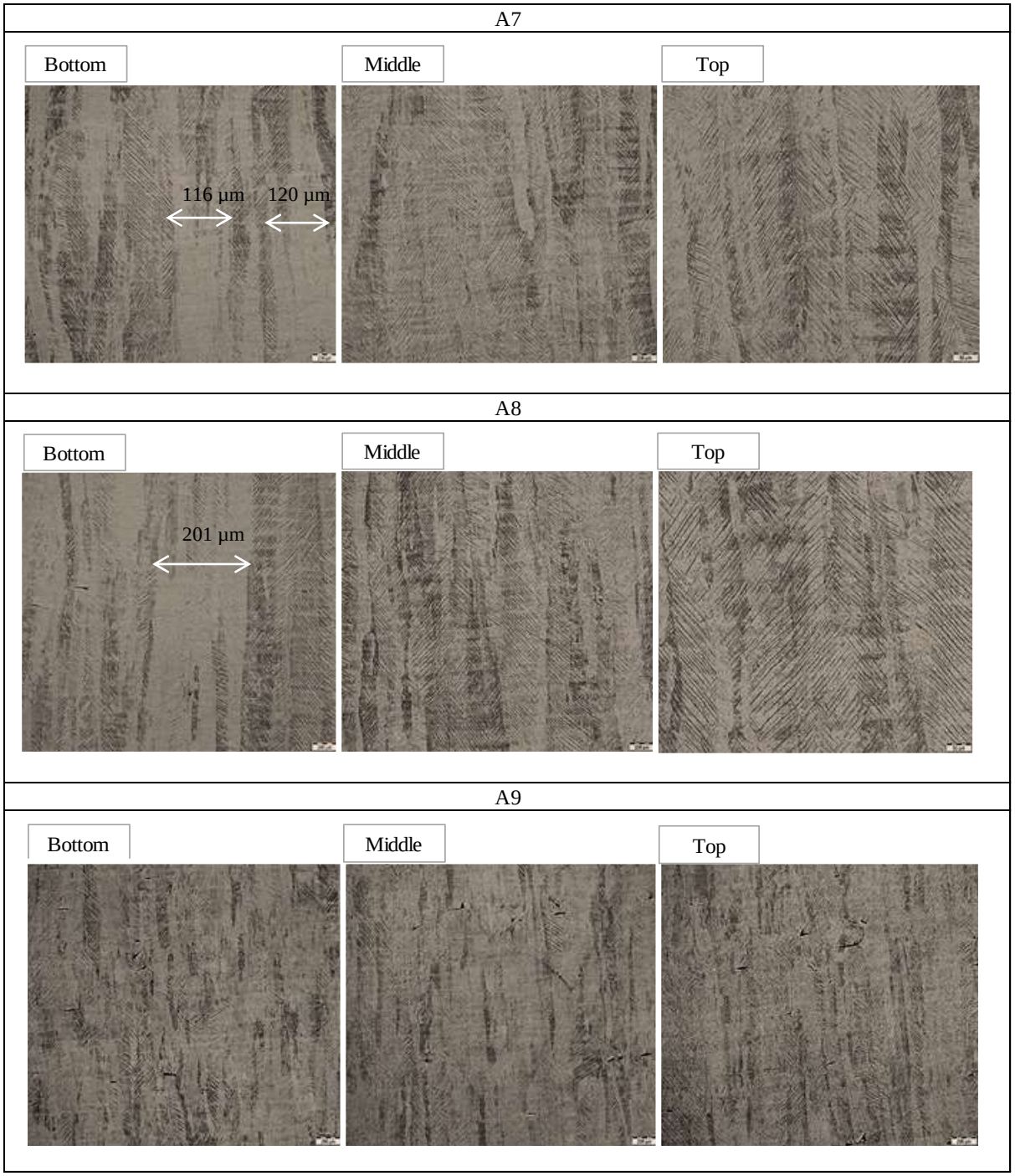

Figure 15: Microstructures of samples manufactured at 1 kW laser power, 3, 3.5 & 4 m/s, 0.10 mm hatch spacing scanning speed and decreasing energy density (67, 57 & 50) J/mm^3. The scale bar indicates 10x Magnification

In Figure 15 similar observations were made as in Figure 13 indicating martensitic microstructures with alpha laths filling columnar prior beta grains. It can be seen that the spread or size of the columnar beta grains in sample A7 and A8 is wider than it is in A9 (produced at high scan speed and low energy density), with sample A8 shown to range from 59 to 201 µm. Sample A9 had a higher level of micro porosity as compared to sample A7 and A8.

4.2 Trial 2 Results: Microstructure as a function of process parameters

The second trail was conducted using a constant layer thickness 0.05 mm, 450 µm spot size, 2 - 3 kW laser power, varied scanning speed and hatch spacing. Micrographs of these samples are presented in Figure 16 and 17. In Figure 16 sample (B1) and (B2), the energy density was varied between 42 to 83 J/mm^3, low energy density resulted in high porosity. The same was observed in Figure 17 and 18. However, it was also noted that too high energy density 150 & 200 J/mm^3 induces micro porosity. Porosity increased with increasing scanning speed and hatch spacing, similar to the behaviour observed in Trial 1.

The microstructure of the samples in trial 2 was also observed to be of acicular α martensite within columnar prior β grains. The alpha laths within prior columnar beta grains were not as pronounced and visible in sample B3 and B1, Figure 16 & 17. The prior beta grains appeared wider at higher energy densities in all cases.

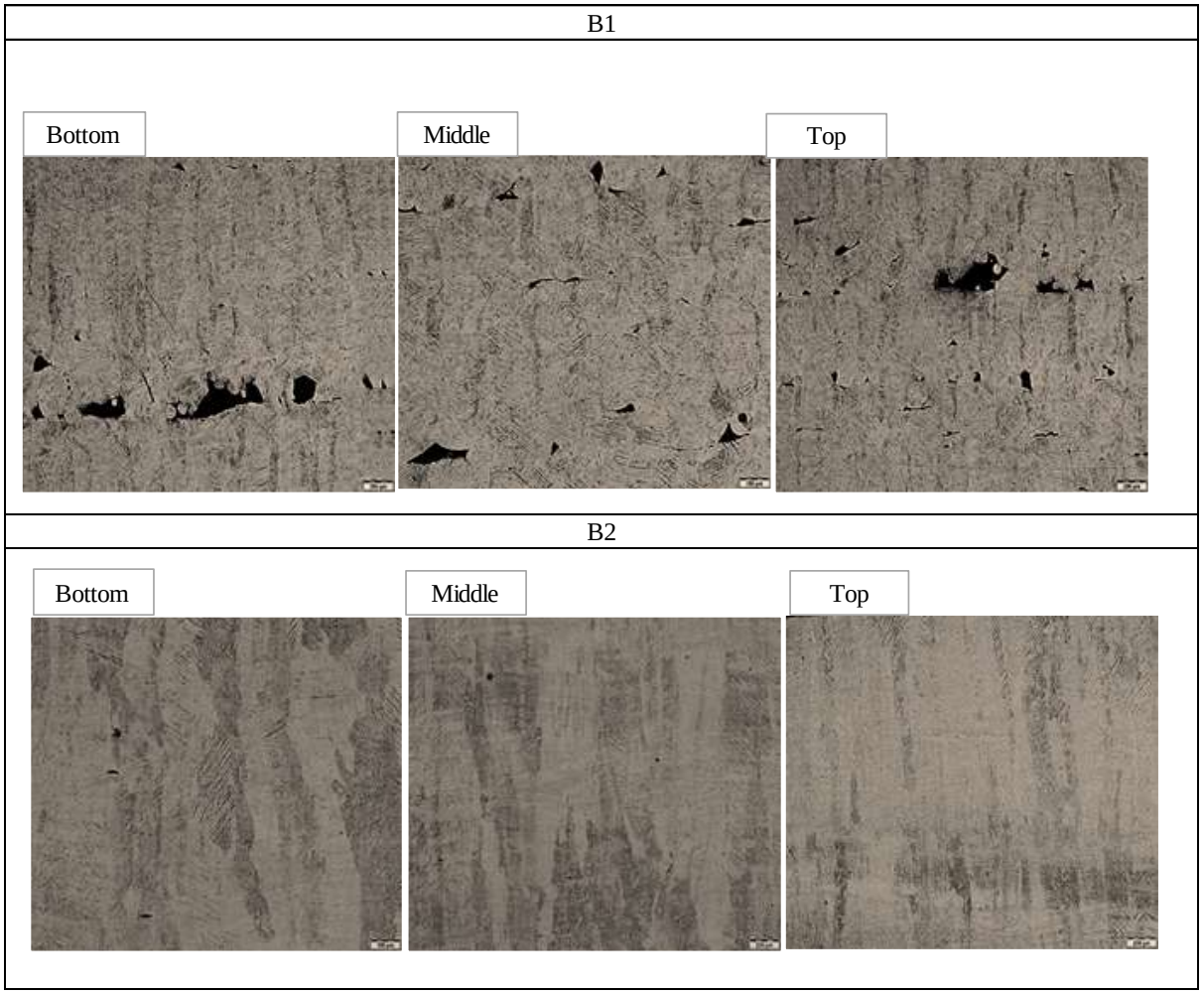

Figure 16: Microstructures of samples manufactured at constant laser power 2 kW, 4 & 2 m/s scanning speed, spot size 450 µm and 0.24 mm hatch spacing, energy density for sample B1 (42 J/mm^3) and B2 at (83 J/mm^3). The scale bar indicates 10x Magnification

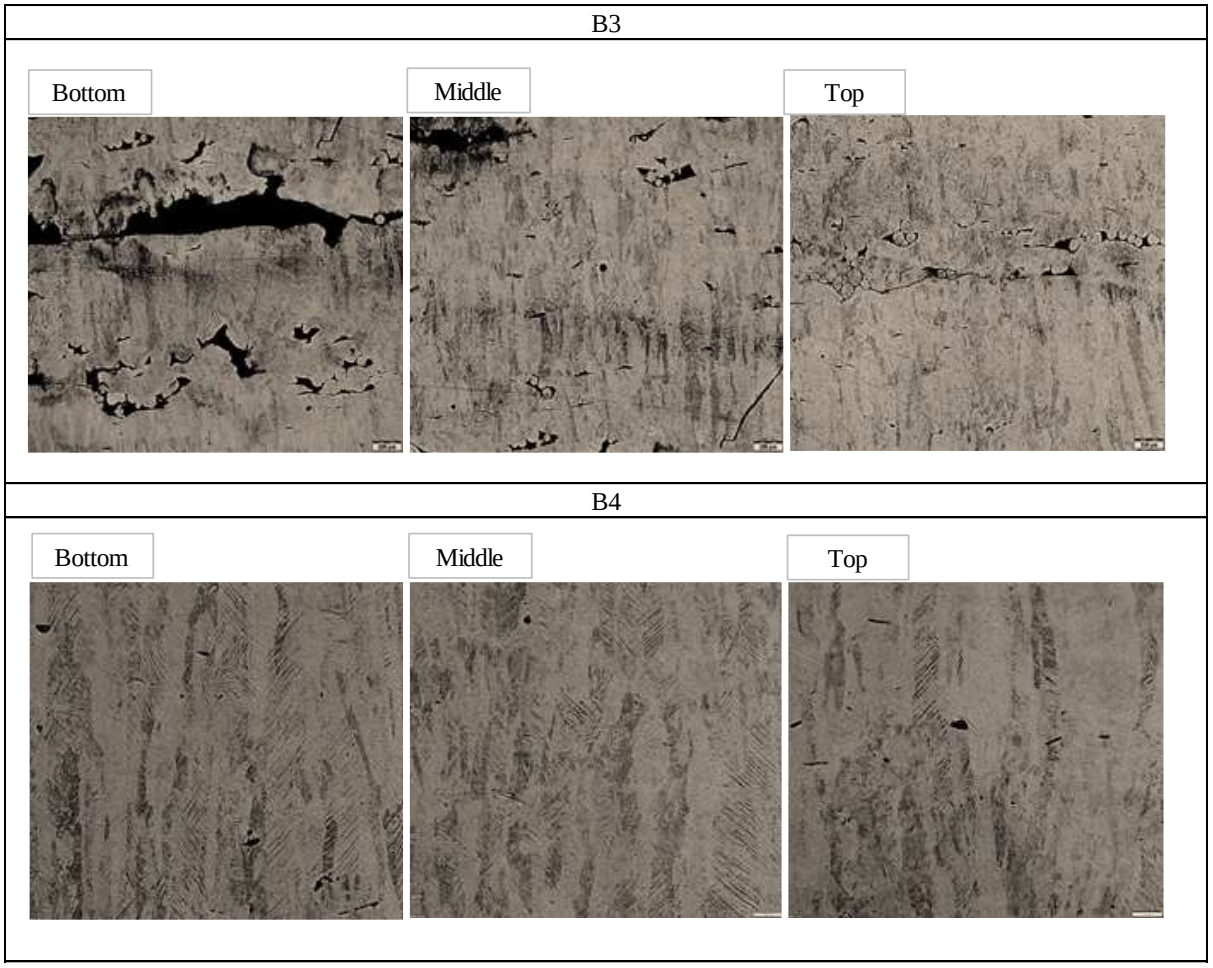

Figure 17: Microstructures of samples manufactured at constant laser power 2 kW, 4 & 2 m/s scanning speed, spot size 450 µm and 0.10 mm hatch spacing; energy density for sample B3 (100 J/mm^3) and B4 at (200 J/mm^3). The scale bar indicates 10x Magnification

In Figure 17, comparing sample B3 and B4 manufactured at high scanning speed (4 m/s) and low and high energy density produced similar results as in Trial 1. Lower energy density resulted in high porosity.

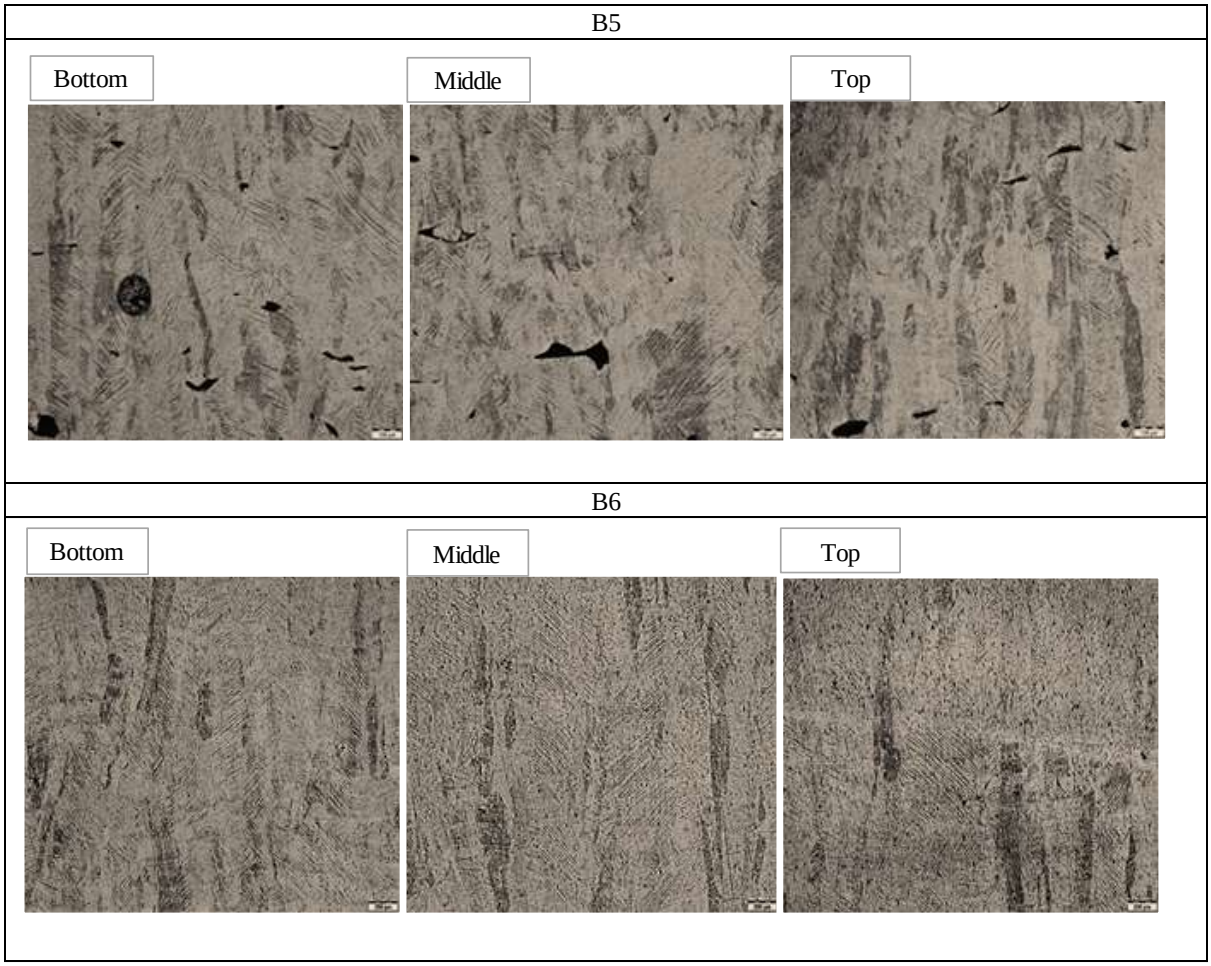

Figure 18: Samples manufactured at constant laser power 3 kW, 4 m/s scanning speed, spot size 450 µm and 0.24 & 0.10 mm hatch spacing; Energy density sample B5 (62 J/mm^3) and B6 at (150 J/mm^3). The scale bar indicates 10x Magnification

From Figure 18, a higher hatch spacing (0.24 mm) in B5 resulted in high fraction porosity as opposed to B6 (0.10 mm). The columnar grains were also wider in B6 than in B5.

Table 5 summarizes porosity measurements taken from all the samples. It should be noted that the porosity value reported in Table 5 is the average of three separate density measurements. The individual density measurements are reported in Table 16 in the appendix, with the porosity values calculated from individual density measurements. The range in porosity values (that is, the difference between the highest measured porosity value and the lowest measured porosity value) are reported for every sample, in the same table. Finally, the ratio (range in measured porosity values): (average porosity) is noted in Table 16. The ratio of the range in measured porosity to the average porosity (the relative range in porosity values) is an indication of the uncertainty in measurement of the porosity value. This ratio is plotted against the average porosity in Figure 19. Generally, the relative range in porosity values decreased with a higher porosity level. At a measured porosity level of about 1%, the relative range was typically about 0.25. If the measured porosity level was between 1 and 2%, the relative range was

between 0.02 and 0.18. For porosity above 2%, the relative range was never above 0.10, and usually below 0.05.

From the results reported in this table, graphical representation of the average porosity as a function of energy density and scanning speed were drawn. See Figure 20 - 21

Table 5: Porosity measurement results

	Sample ID	Power (kW)	Spot Size (µm)	Scanning Speed (m/s)	Hatch Spacing (mm)	Energy density (J/mm3)	Ave Density (g/cm3)	% Density	% Porosity
Trial 1	**A1**	1	250	3	0.13	51	4.39	99.12	0.88
	A2	1	250	3.5	0.13	44	4.36	98.42	1.58
	A3	1	250	4	0.13	38	4.35	98.18	1.82
	A4	1	250	3	0.15	44	4.39	99.07	0.93
	A5	1	250	3.5	0.15	38	4.37	98.62	1.38
	A6	1	250	4	0.15	33	4.29	96.82	3.18
	A7	1	250	3	0.10	67	4.37	98.56	1.44
	A8	1	250	3.5	0.10	57	4.35	98.26	1.74
	A9	1	250	4	0.10	50	4.34	97.97	2.03
Trial 2	**B1**	2	450	4.0	0.24	42	4.16	93.84	6.16
	B2	2	450	2.0	0.24	83	4.40	99.39	0.61
	B3	2	450	4.0	0.10	100	4.34	97.90	2.10
	B4	2	450	2.0	0.10	200	4.35	98.22	1.78
	B5	3	450	4.0	0.24	63	4.31	97.31	2.69
	B6	3	450	4.0	0.10	156	4.38	98.89	1.11

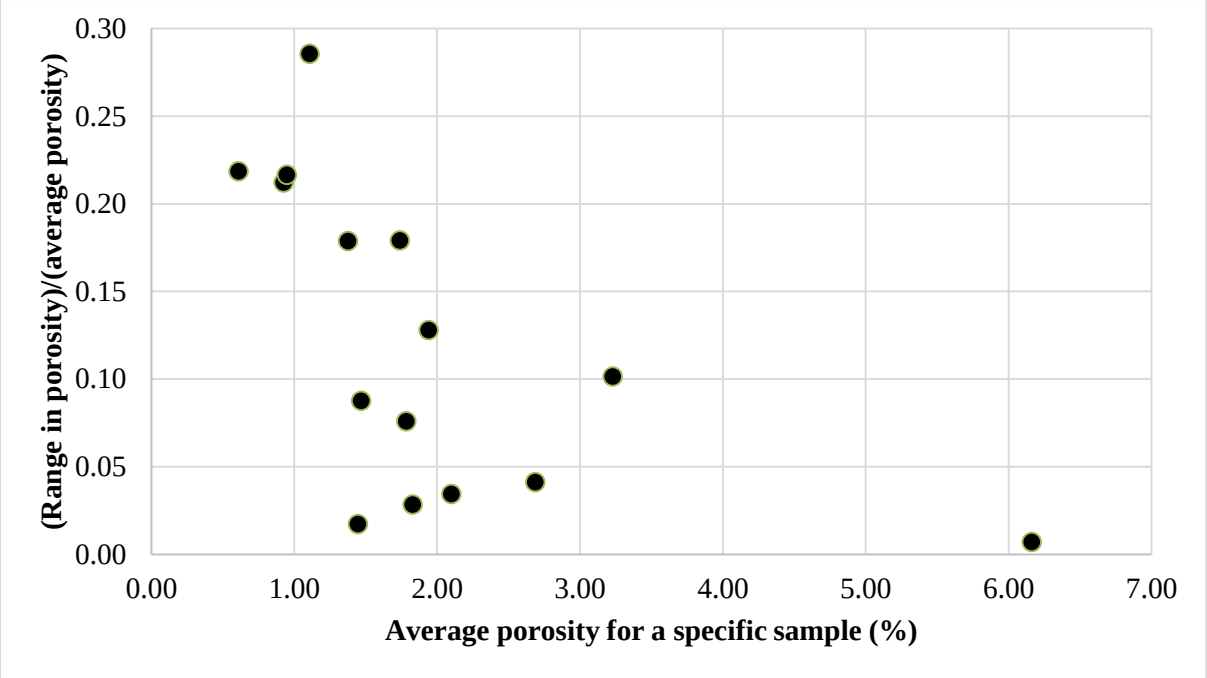

Figure 19: Range in porosity/ average range porosity vs. average porosity for a specific sample

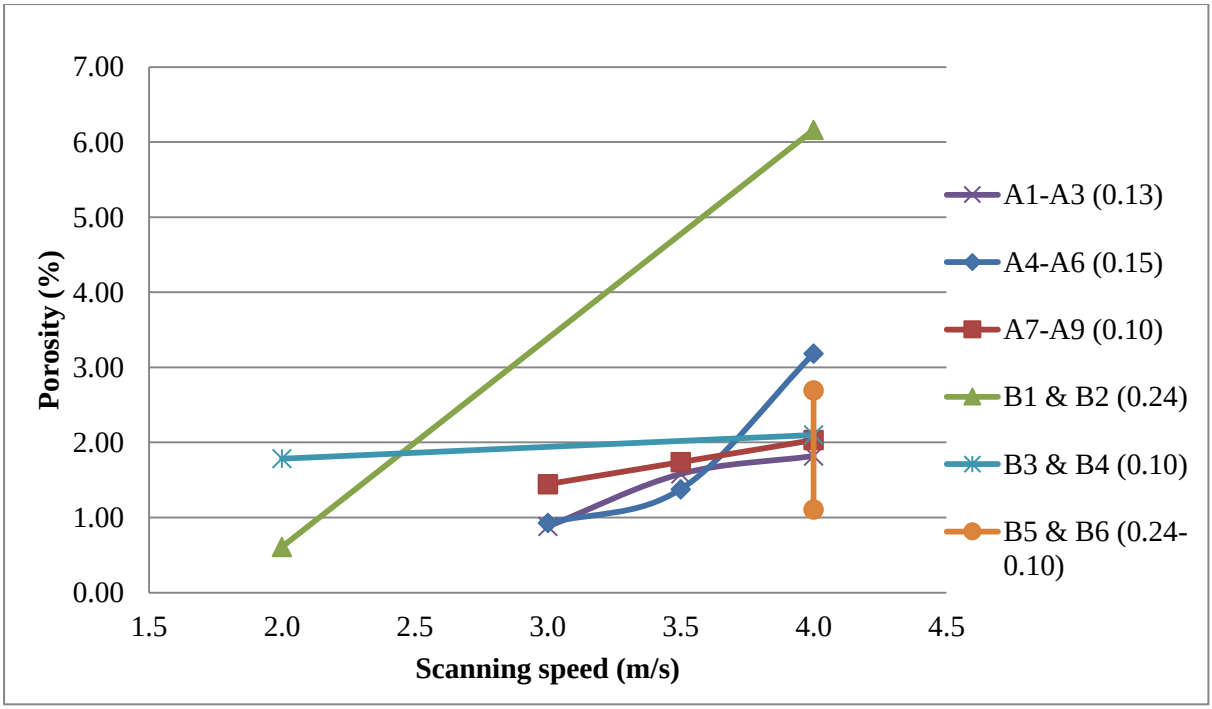

Figure 20: Effect of scanning speed and hatch spacing on porosity: Porosity map for A & B series samples. The figure in brackets indicates the hatch spacing in mm. All measured values of porosity are shown, regardless of laser power

The effect of scanning speed and hatch spacing illustrated in Figure 20, also demonstrated how porosity increases with increasing scanning speed and hatch spacing. The lowest % porosity recorded in the first trial samples at 1 kW was 0.88% as opposed to 0.61% at 2 kW. In terms of hatch spacing, the highest % porosity (3.18%) was attained at 0.15 mm highest hatch spacing compared to 0.10 mm hatch spacing for the A-series trial samples. The B-series trial samples recorded the highest porosity of 6.2% for sample B1 manufactured at the highest scanning speed of 4 m/s, and at the 0.24 µm highest hatch spacing.

The effect of energy density illustrated in Figure 21 indicated that porosity decreases with increasing energy density for both series A and B. Similar as noted by previous authors [Gong et al. (2013) & Kasperovich et al. (2016)], for the same energy density, a range of porosity values was observed.

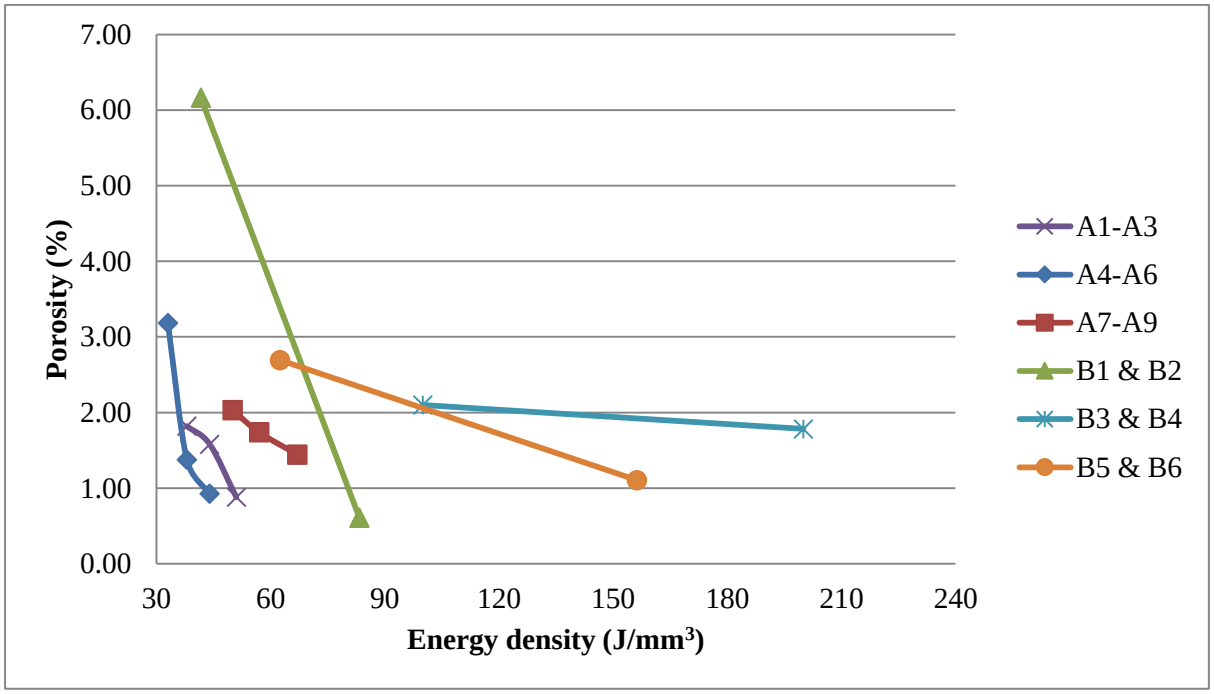

Figure 21: Effect of energy density and hatch spacing on porosity: Porosity map for (A & B) series samples

4.3 Microstructures of trial 1& 2 samples

The SEM images presented in Figure 22 to 25 were taken to compare the microstructure obtained at low laser power of 1 kW, and at 2 – 3 kW laser power increasing energy density. A general observation made, was that for all samples the microstructure was martensitic. The only major difference in the structure of the different samples was the amount of porosity. Small round pores were seen in samples manufactured at a high laser power of 2 -3 kW, regardless of the energy density. See arrows indicating round pores in Figure 25.

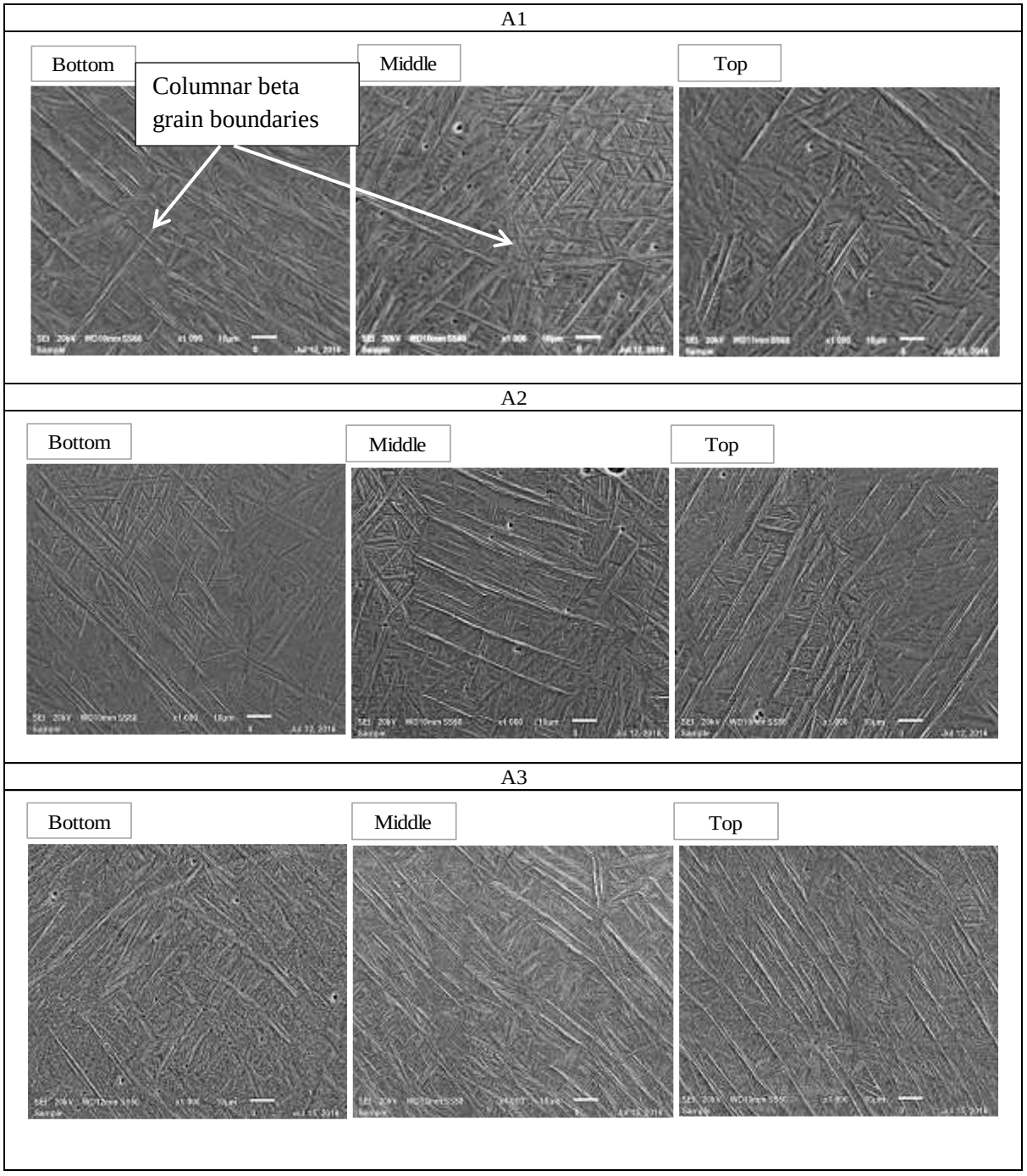

Figure 22: Trial 1 SEM microstructures of samples manufactured at 1 kW low laser power, 3, 3.5 & 4 m/s scanning speed, 0.13 mm hatch spacing and decreasing energy density (51, 44 & 38) J/mm^3 at 1000x Magnification

In Figure 22, all microstructures were observed to be martensitic. Columnar grain boundaries are indicated by arrows, with alpha laths clearly visible between prior beta grain boundaries. The columnar grain size in sample A1 and A2 appeared to be much wider than in A3 (manufactured at high scanning speed and low energy density).

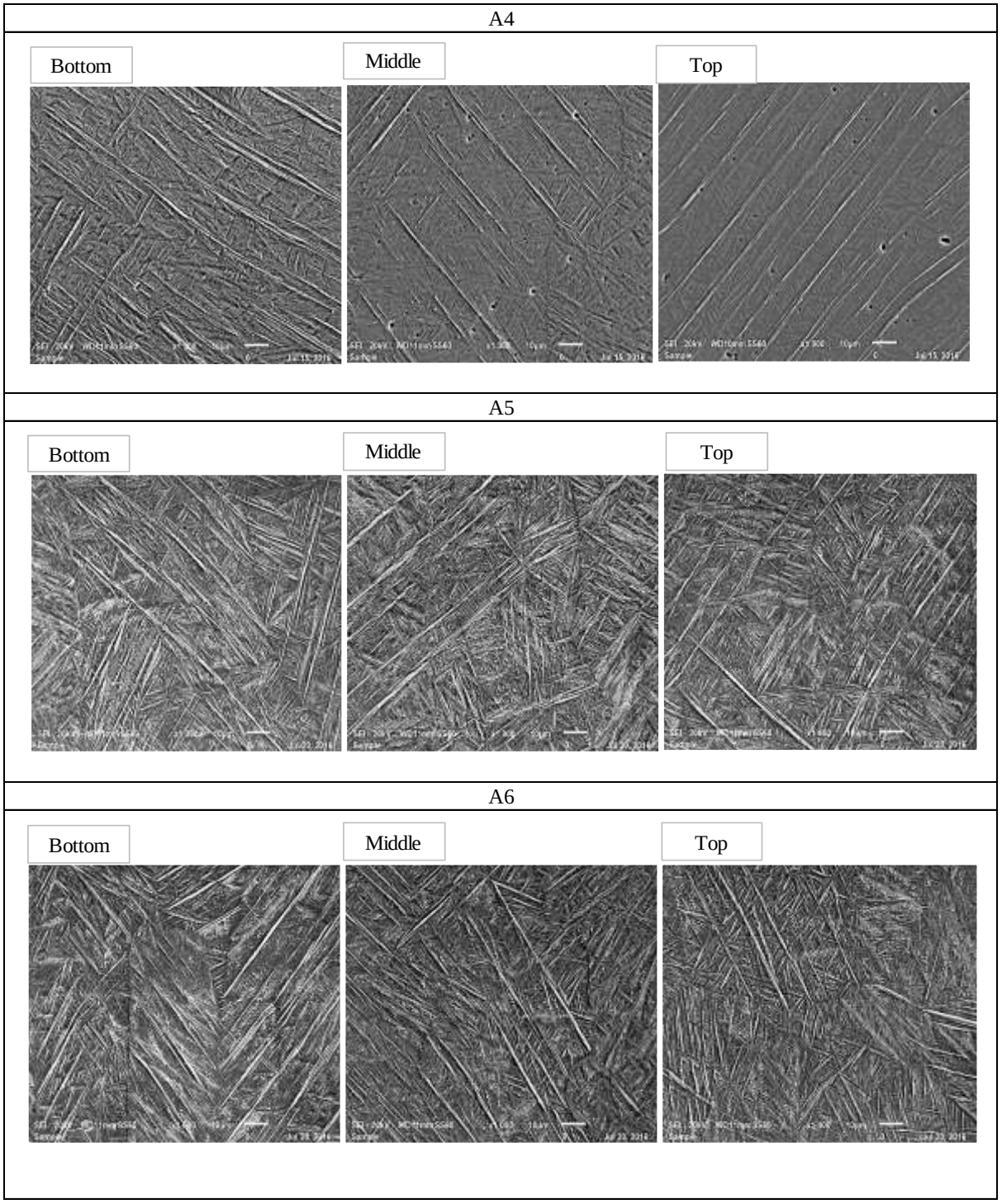

Figure 23: Trial 1 SEM microstructures of samples manufactured at 1 kW low laser power, 3, 3.5 & 4 m/s scanning speed, 0.15 mm hatch spacing and decreasing energy density (44, 38 & 33) J/mm^3 at 1000x Magnification

The micrographs in Figure 23 and 24 all appear to be martensitic with alpha laths clearly visible within prior beta grain boundaries. As seen in Figure 14 sample A5 and A6 contained some un-melted powder residue compared to sample A4, which could have resulted from insufficient powder melting due to the low energy density (38 and 33 J/mm^3), as seen in Figure 14.

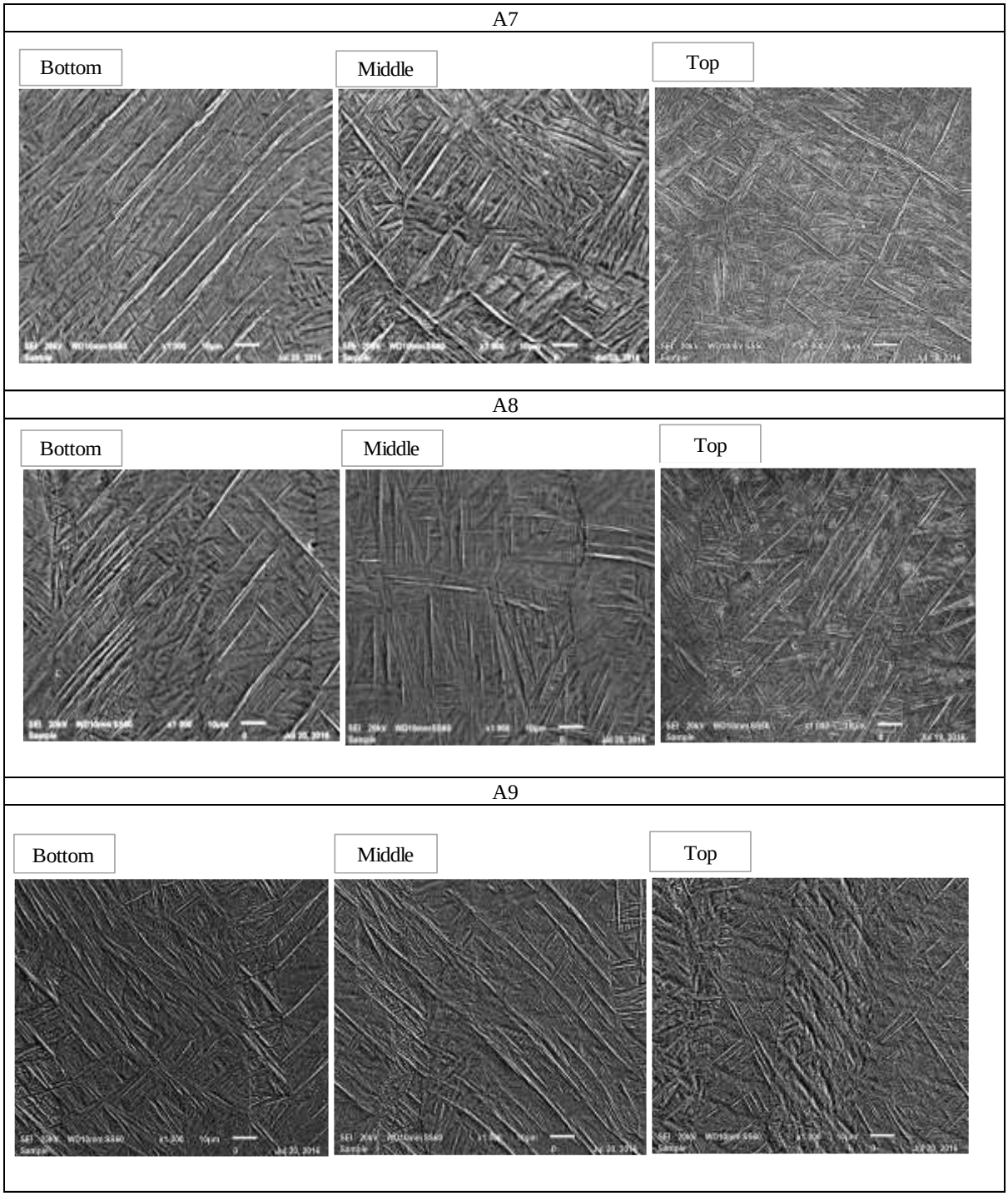

Figure 24: Trial 1 SEM microstructures of samples manufactured at 1 kW low laser power, 3, 3.5 & 4 m/s, 0.10 mm hatch spacing scanning speed and decreasing energy density (67, 57 & 50) J/mm^3 at 1000x Magnification

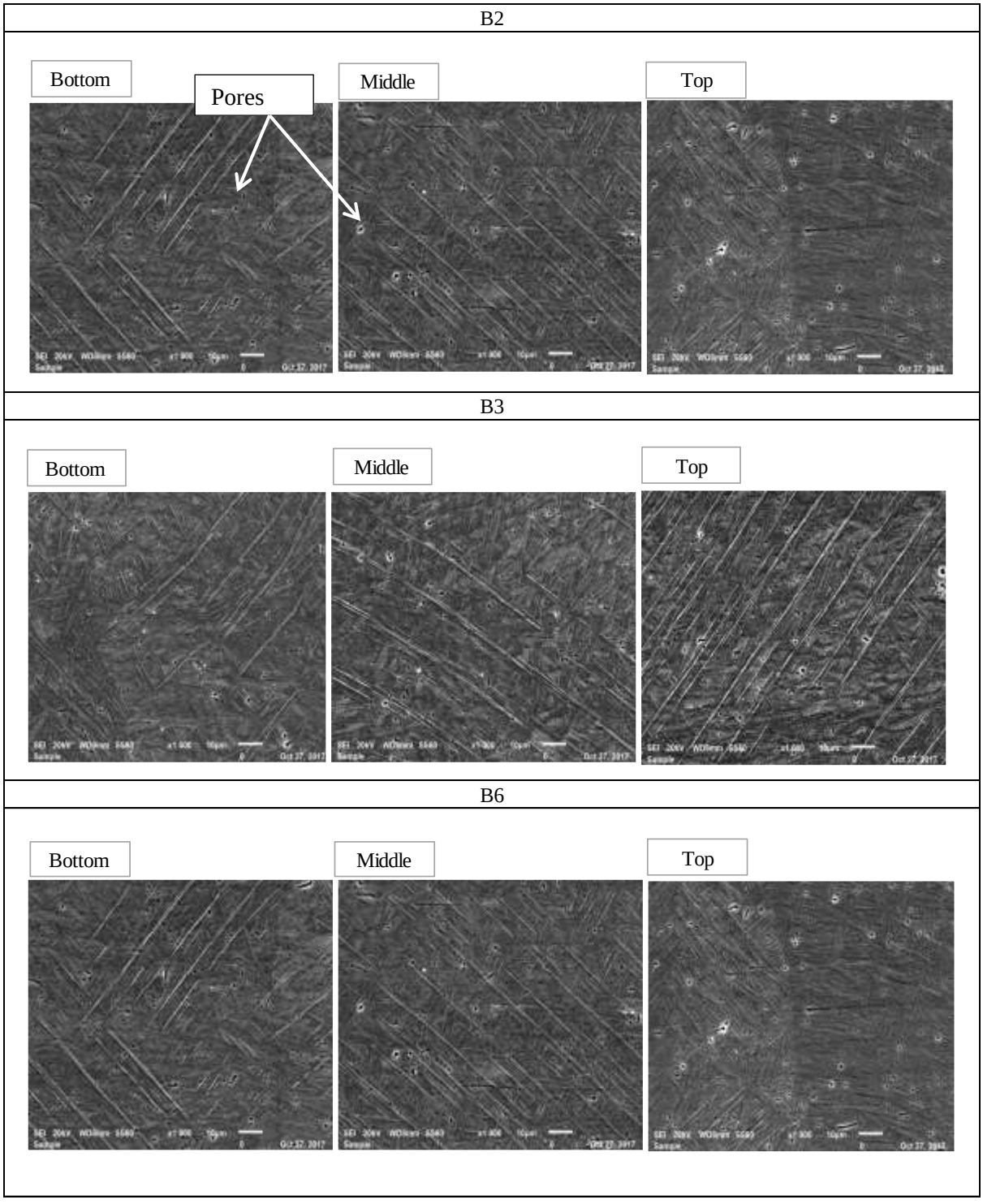

Figure 25: Trial 2 SEM microstructures of samples manufactured at 2 to 3 kW high laser power, 2 & 4 m/s scanning speed , 0.10 & 0.24 mm hatch spacing and increasing energy density (83, 100 & 156) J/mm^3 at 1000x Magnification

4.4 EBSD analysis

EBSD analysis of samples manufactured at a high and a low laser power, and at a high and at a low energy density was done. Figure 26 represented sample A1 manufactured at 1 kW laser power, 51 J/mm^{3}energy density, whilst Figure 27 sample B3 manufactured at 2 kW 100 J/mm^3 energy density and Figure 28 sample B6 manufactured at 3 kW laser power, 156 J/mm^3 energy density. At low laser power beta phase was detected to be at about 0.2% compared to high laser power 2 and 3 kW, which was found to have increased to 1.2 and 5.5 % respectively, the alpha phase remaining as a balance. The alpha grain size indicated a slight increase with increase in laser power and energy density, comparing the 3 samples (16 µm, 17 µm and 20) µm reported in Table 6.

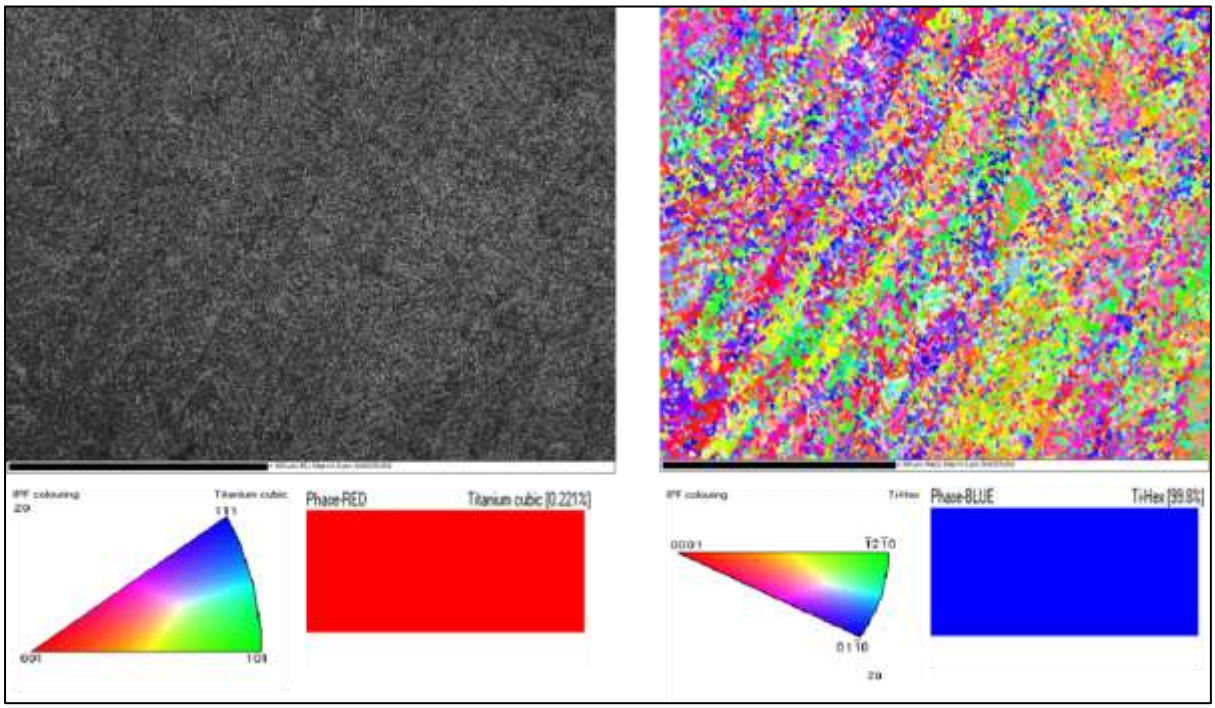

Figure 26: Phase analysis sample A1 manufactured at 1 kW laser power, 3 m/s scanning speed, 0.13 mm hatch spacing, 51 J/mm^3 energy density, and 250 µm spot size

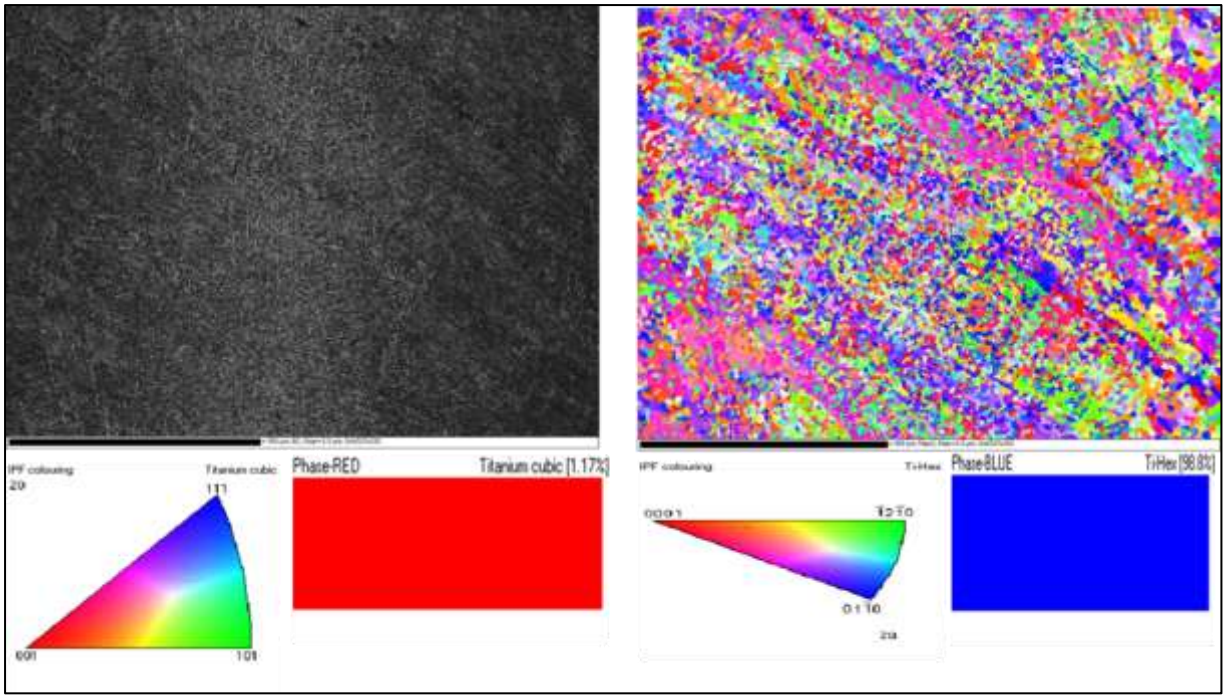

Figure 27: Phase analysis sample B3 manufactured at 2 kW laser power, 4m/s scanning speed, 0.10 mm hatch spacing, 100 J/mm^3 energy density, and 450 µm spot size

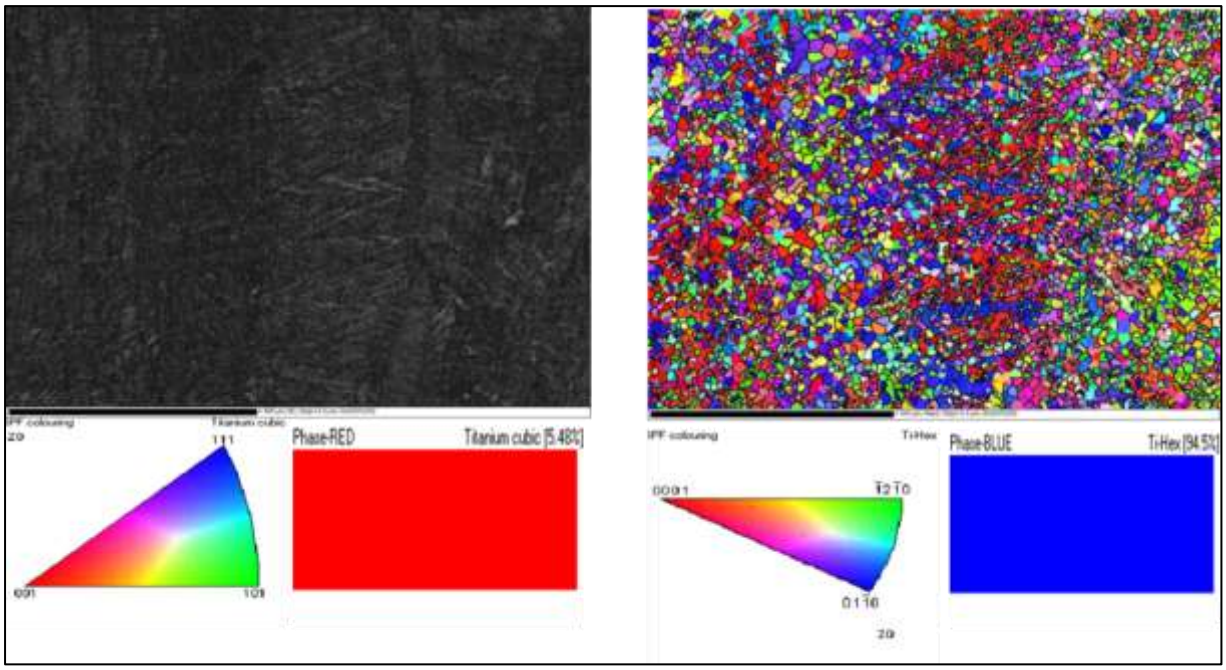

Figure 28: Phase analysis sample B6 manufactured at 3 kW laser power, 4m/s scanning speed, 0.10 mm hatch spacing, 156 J/mm^3 energy density, and 450 µm spot size

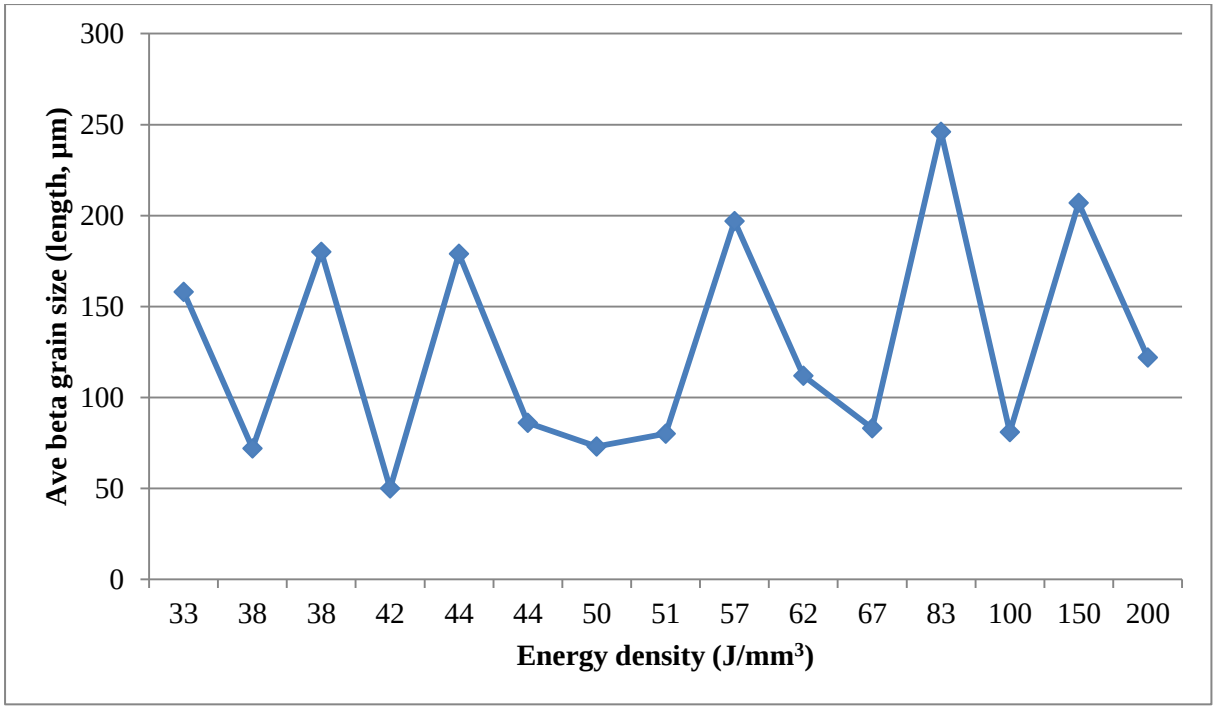

Figure 29: Average beta grain size as a function of energy density

Within the set of parameters used, Figure 29 and 30 indicated an increase in the average beta grain size with increase in energy density, where-as in Figure 30 the average alpha length grain size indicated a decrease with increasing energy density.

Table 6: EBSD Phase fraction and alpha grain size results

	Parameters	A1	B3	B6
	Energy density (J/mm^3)	51	100	156
	Laser power (kW)	1	2	3
Phase fraction	Titanium β (%)	0.22	1.17	5.49
	Titanium α (%)	99.8	98.8	94.5
Alpha grain size measurements	Minimum length of average α grain(µm)	12.5	12.5	12.5
	Maximum length of average α grain (µm)	60.3	59	94.9
	Standard deviation (µm)	4.4	5.1	7.9
	No. of grains	1972	2019	2369
	Range in length of α grain (µm)	25.6 - 31.8	21.1 - 29.1	18.2 - 19.2

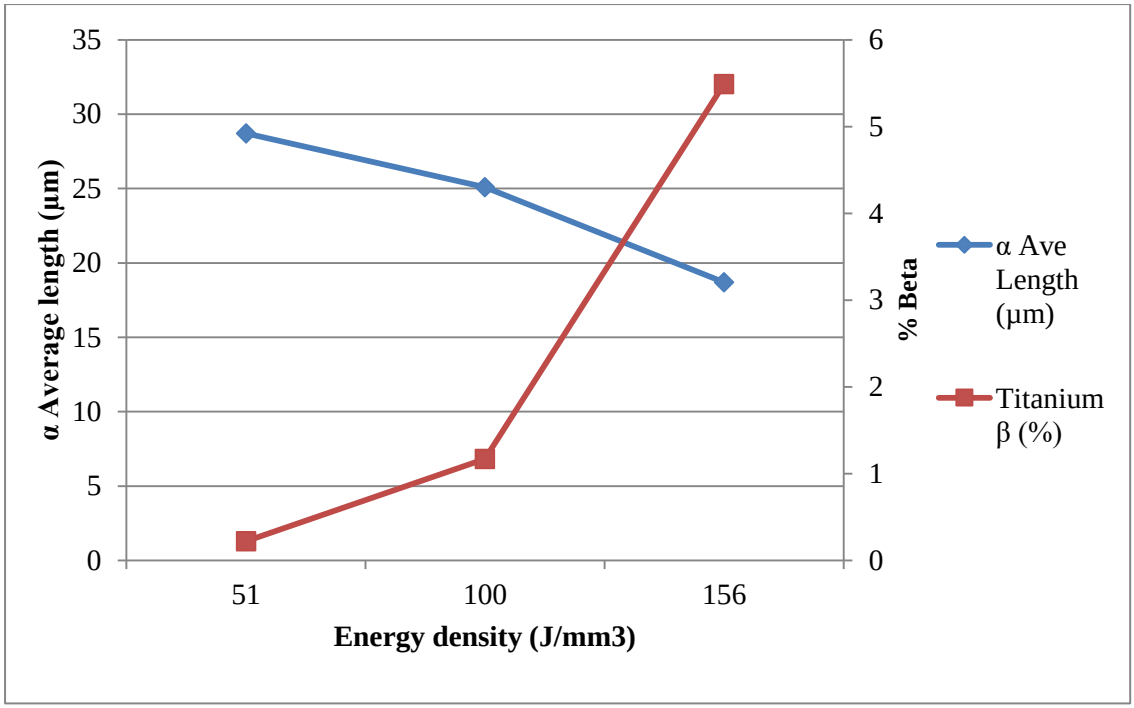

Figure 30: Relationship between α average length, and % Beta with increasing energy density

4.5 Hardness

Vickers hardness measurements were conducted on all the built samples, except samples A5 and A6 that were not characterised due to the high level of macro porosity. First trial (HV 300 g) hardness measurements results for low laser power samples A1 - A3 were reported to be in a range of 359 - 389 in Figure 31, samples A7 - A9 were reported to be in a range of 343 - 383 in Figure 32.

Second trial (HV 300 g) hardness measurements results for high laser power samples B1and B2 were reported to be in the range of 329 - 418 in Figure 33, B3 & B4 (332 - 357) in Figure 34, and B5 & B6 range of (316 - 418) Figure 35. The 1st initial layers from the build platform for all samples indicated high hardness trend decreasing with more layers added further away from the build platform in Figure 36.

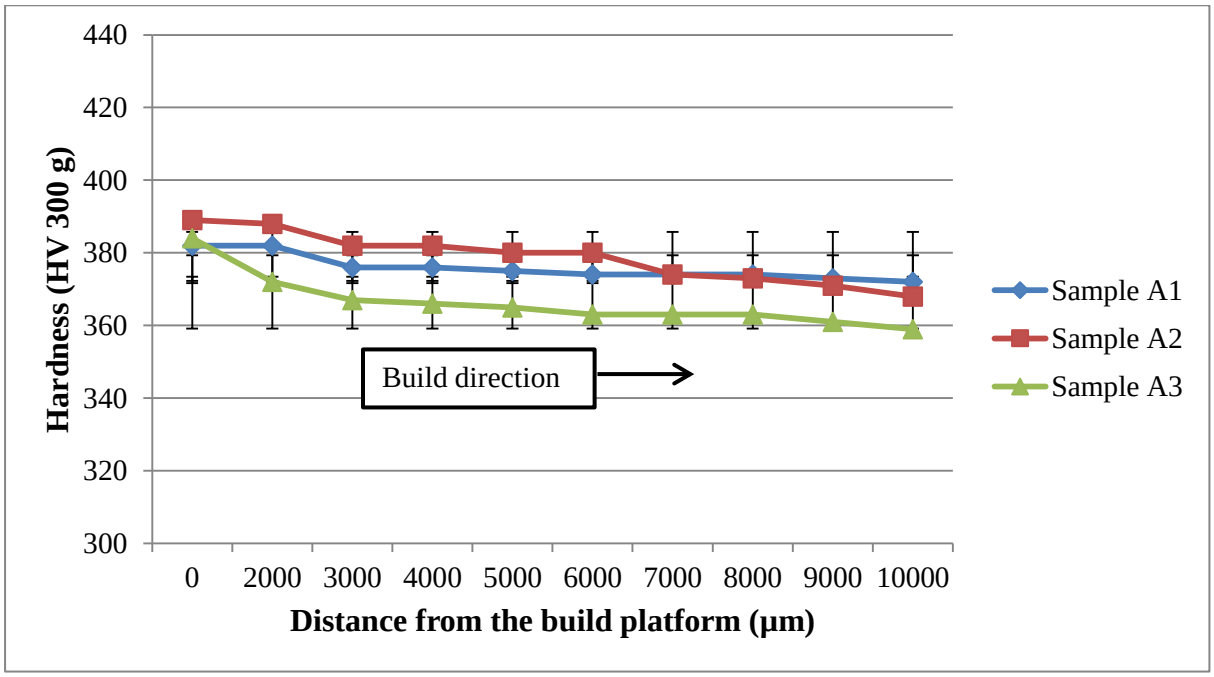

Figure 31: Hardness values as function of distance from the build platform for samples manufactured at constant 1 kW laser power, 0.13 mm hatch spacing 250 µm spot size, varied scanning speed (3, 3.5 & 4 m/s), and energy density range (51-38) J/mm^3

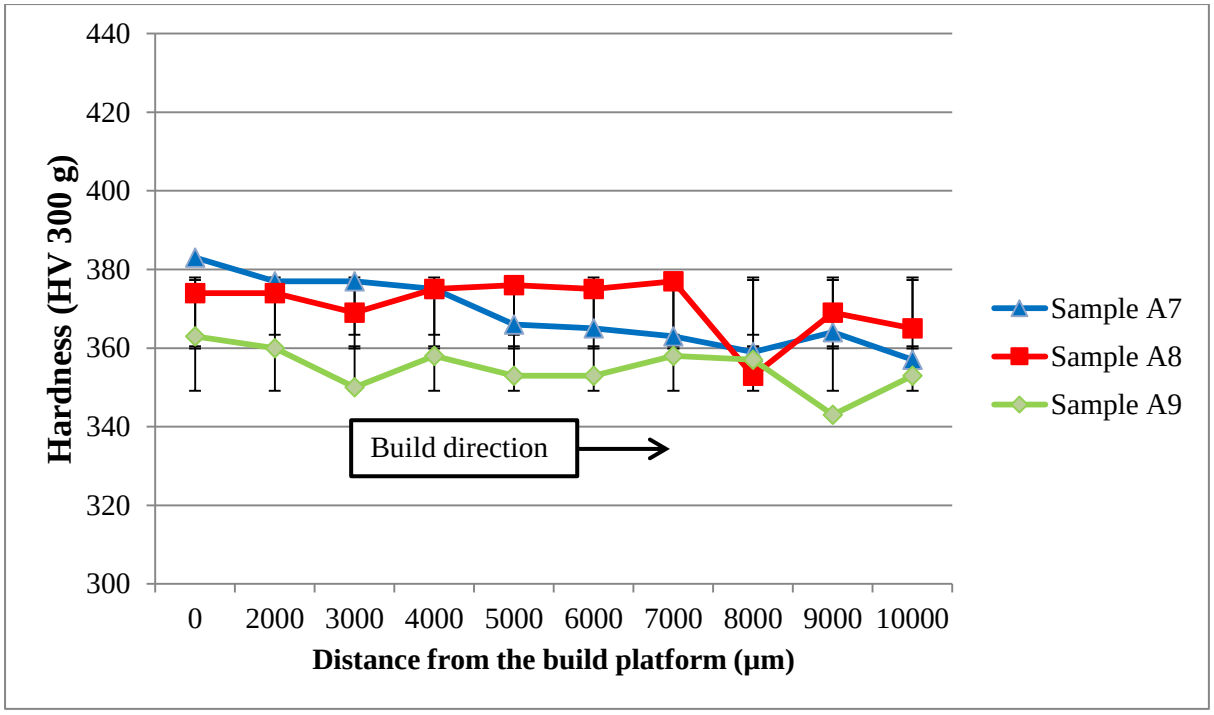

Figure 32: Hardness values as function of distance from the build platform for samples manufactured at constant 1 kW laser power, 0.10 mm hatch spacing 250 µm spot size, varied scanning speed (3, 3.5 & 4 m/s), and energy density range (67-50) J/mm^3

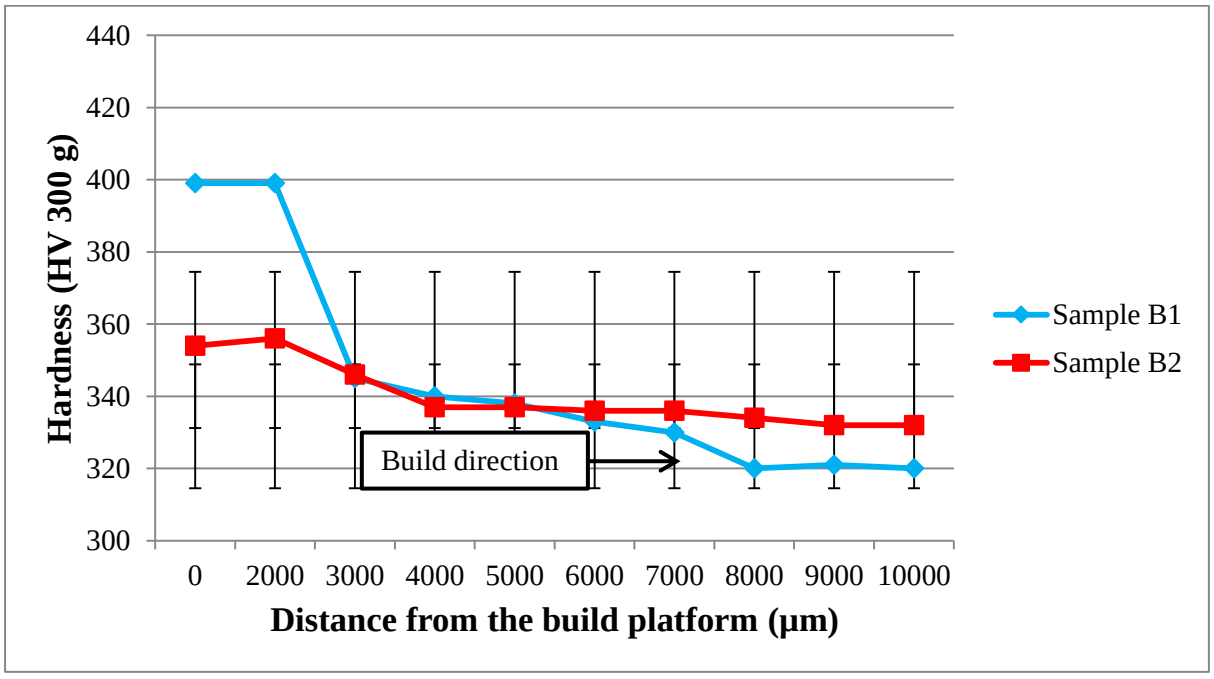

Figure 33: Hardness values as function of distance from the build platform for samples manufactured at constant 2 kW laser power, 0.24 mm hatch spacing, varied scanning speed 4 & 2 m/s, 450 µm spot size, and energy density range (42-83) J/mm^3

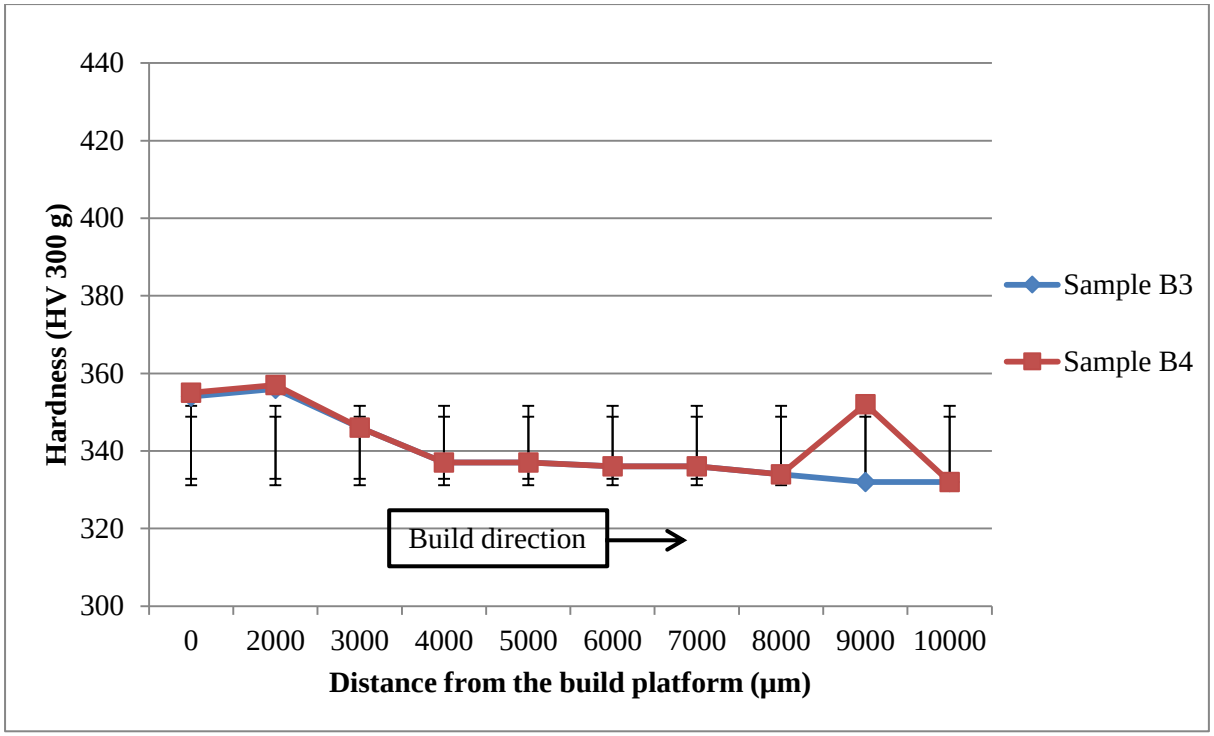

Figure 34: Hardness values as function of distance from the build platform for samples manufactured at constant 2 kW laser power, 0.10 mm hatch spacing, varied scanning speed 4 & 2 m/s, 450 µm spot size, and energy density range (100-200) J/mm^3

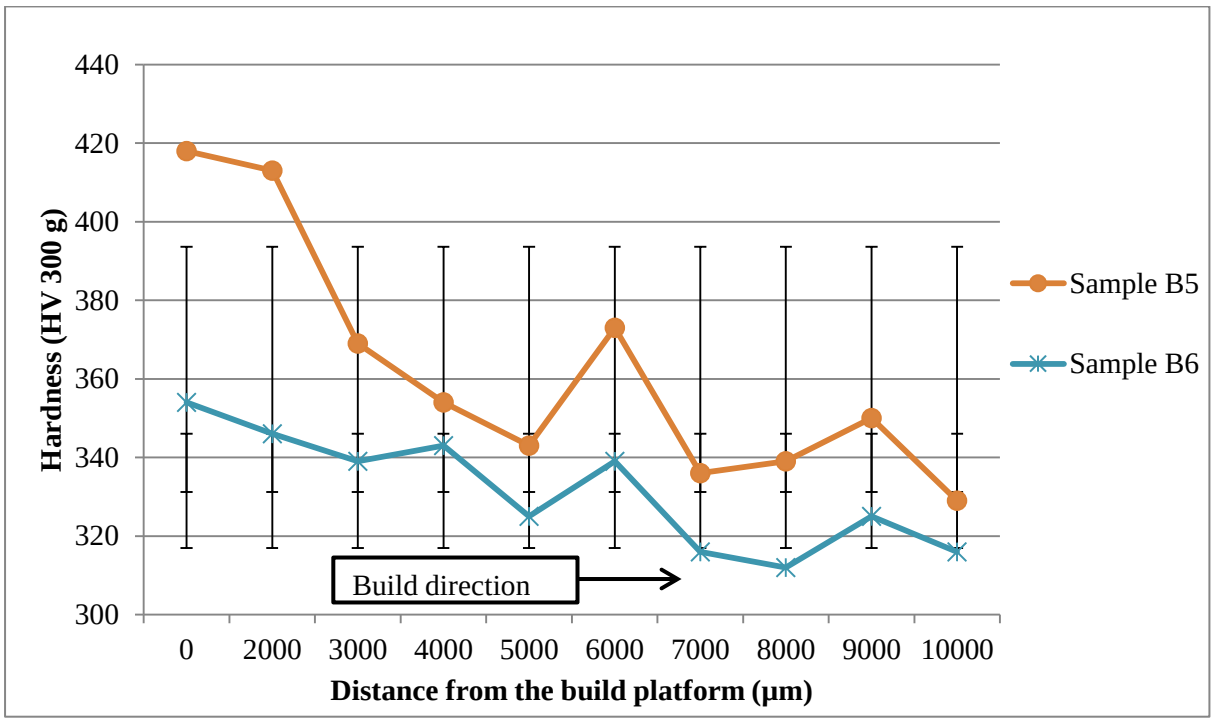

Figure 35: Hardness values as function of distance from the build platform for samples manufactured at constant 3 kW laser power, 4 m/s scanning speed, varied hatch spacing 0.24 & 0.10 mm, 450 µm spot size, and energy density range (63-156) J/mm^3

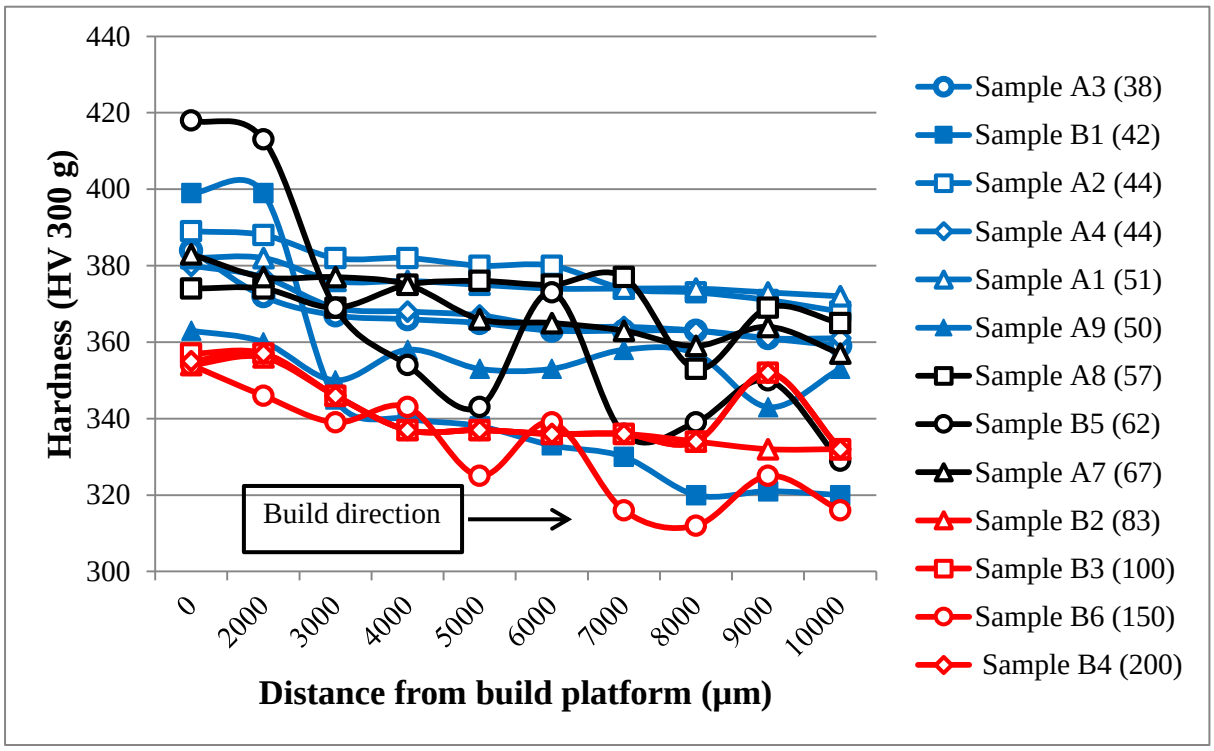

Figure 36: Combined hardness measurements with different levels of energy density (below 55 J/mm^3, blue, 55 to 80 J/mm^3 black, above 80 J/mm^3 red, values in brackets indicate energy densities per sample. In brackets values 38-200 indicating energy densities (J/mm^3)

5. DISCUSSION

In this chapter, the experimental results, specifically the response of porosity, microstructure and hardness to changes in individual processing parameters (laser power, scanning speed, hatch spacing, spot size and energy density) are discussed. The results of a statistical analysis describing the combined effect in changes in the processing parameters are also set out.

5.1 Porosity

The L-PBF built metallic parts were observed to have variable porosity, similar to findings in various publications (Sames et al. 2016), (Kasperovich et al. 2016) & (Gong et al. 2013). The fraction porosity was based on density measurements and reflected both micro and macro pores (observed using an optical microscope at (20x magnifications) and micro-porosity (observed using the SEM at 1000x magnification).

The range in individual estimates of the porosity of the sample generally decreased with a higher porosity level (Figure 19). The lower relative range at higher levels of porosity may indicate that the measurement technique used during this study yielded reliable estimates for porosity if the porosity was above about 2% (with a relative range of 0.10 or lower). For lower levels of porosity, the estimate was subjected to more variation. The high relative range in estimates for the porosity of a sample at lower values of porosity may be an indication that density measurements may not be the optimal technique to measure levels of porosity below about 1%.

The following observations due to changes in process parameters were made:

- Laser power: At a specific energy density, a high laser power resulted in an increase in micro pores. Most micro pores were round and likely to be gas porosity. The formation of gas pores is likely to be favored by high laser power resulting in over-heating of the liquid melt pool, metal gas evaporation, and re-solidification (Vilaro, 2011 & Attar, 2014). The parts manufactured using a high laser power of 2 to 3 kW appeared on the SEM microstructures to have a high fraction of round pores compared to samples manufactured at 1kW laser power, see Figure 22 to 25. From the set of parameters used, the highest fraction porosity attained at 2 kW was about 6% whereas at 1 kW it amounted to 3% (Table 5 and Table 16 in the appendix).
- Scanning speed: the higher the scanning speed, the higher the porosity, results correlated to investigations by others (Gong et al. 2013 & Kasperovich et al. 2016). For example, samples that were manufactured at constant 1 kW laser power with 0.10 µm constant hatch spacing and increasing scanning speed 3, 3.5 and 4 m/s resulted in an increased porosity of 1.4 to 2%, see (Figure 20). The same effect was observed with increasing scanning speed at 2 kW as the porosity also increased from 0.6 to 6%.

- Hatch spacing: the bigger the hatch spacing, the higher the porosity. PBF process simulations by (Tang et al, 2017) also predicted that porosity and rates of porosity increases with higher beam speed, hatch spacing, or layer thickness. A hatch spacing of 0.24 mm resulted in 3% average fraction porosity whereas 0.10 mm hatch spacing resulted in 1.7% average fraction porosity, see results in Table 5.
- Energy density: Generally, high energy density results in lower porosity see microstructure as a function of energy density and scanning speed (Figure 13 – 15). Samples manufactured at a constant 1 kW laser power and 0.15 mm hatch spacing with an increase in energy density from 33 to 44 J/mm^3 resulted in a decrease in fraction porosity from about 3 to 1% by volume, see graph illustration in Figure 21. Samples manufactured at a constant laser power of 2 kW, hatch spacing 0.24 mm had a similar decrease in porosity, from 6 to 0.6 volume percent as the energy density increased from 42 to 83 J/mm^3, Figure 16 & 17. However, it was also noted that too high or excessive energy density increases micro round porosity, see Figure 24 (energy densities in the range of 83 to150 J/mm^3). Findings by Gong et al. (2013) & Kasperovich et al. (2016) also indicated that insufficient low energy density results in increased porosity.

5.2 Microstructure

Due to high temperature gradients inherently associated with PBF processing, the microstructure of LPBF produced Ti6Al4V is martensitic (Kobryn & Semaitin, 2001) & (Wu et al. 2004). The manufactured parts had a microstructure of acicular α martensite within columnar prior β grains, for all energy density values used during the current study. A small amount of β was invariably present. Wu, et al., also reported that under varied process parameters (laser power, scan speed) columnar prior beta grains dominate the entire solidification structure.

An increase in the energy density resulted in an increase in the volume fraction and size of β as demonstrated with the limited number of EBSD measurements of the volume fraction, as reported in Table 6, Figure 29 & 30. At a low energy density of about 51 J/mm^3 sample A1, 0.2% beta phase was present, Figure 26. An energy density of 100 J/mm^3 sample B3 resulted in 1.2% beta, Figure 27. A further increase in energy density to 150 J/mm^3 sample B6 resulted in 5.5% beta, see Figure 28. The balance was always α martensite. The measured prior beta grain size averaged between 73 to 180 µm at 1 kW, 50-246 µm at 2 kW, 112-207 µm at 3 kW, Table 17 in the appendix. The alpha grain size dimension obtained from the EBSD results, averaged at 16 µm for samples manufactured at 1 kW and increased to 18 µm at 2 kW, whereas the alpha grain dimension at 1 kW averaged at 34 µm and 21 µm at 2 kW, see Table 6. Figure 30 furthermore indicated a decrease in the average alpha length grain size with increasing energy density.

5.3 Hardness

The Vickers micro hardness varied between 320 to 380 HV 300 g, similar to average hardness results reported in literature (Galarraga et al. 2016) & (Koike et al. 2011). Generally the initial layers had a slightly higher hardness than the last deposited layers, see Figure 31-36. The higher hardness of the initial layers was likely due to fast cooling of these layers, as no pre-heating was applied. In general, the high energy density samples are slightly softer (although the energy density seems to be a poor predictor for change in hardness) in Figure 36;

- The low-energy density samples tend to have a larger drop in hardness in the build direction;
- There seems to be a lot of variability on the graph;

The range of hardness was not that narrow; the difference between the highest and the lowest hardness was about 418 to 312 HV. Changes in the processing parameters did not result in a significant difference in the average hardness. Figure 31 & 32 samples manufactured at a laser power of 1 kW had an average hardness in the range of 343 to 389 HV 300 g, whilst samples manufactured at 2-3 kW had an average hardness that was slightly higher, typically 320 to 418 HV 300 g (in Figure 33 to 35 and Table 18 & 19 in the appendix). The constant hardness was in all likelihood associated with a small change in β content (0.2 to 5.5%) over the range of process parameters used. The LPBF process is inherently associated with fast cooling. The absence of pre-heating and or controlled cooling increased the cooling rate, in all likelihood.

5.4 Statistical analysis

From the observed effects of changes in processing parameters on porosity, microstructure and hardness, a statistical analysis to develop a multiple linear regression model of the response of porosity and hardness was conducted. Given the comparatively minor changes in microstructures, the effect of processing parameters on the fraction of β was not considered.

5.4.1 Evaluation of the effect of process parameters on porosity

A multiple linear regression analysis was done on the data obtained from the porosity analysis tests conducted. Porosity was evaluated as a function of the following main parameters:

- Laser power
- Scanning speed;
- Hatch spacing;
- Spot size.

5.4.1.1 Analysis of variance test

The analysis of variance technique was used to determine if there were any statistically significant differences between the means of the independent variables. For a multiple linear regression model to be considered statistically significant, the p-value must be < 0.05 (Fisher, 1973). In this case the test resulted in a p-value of 0.019 in Table 7, indicating that there was a statistically significant linear relationship between the set of predictors (i.e. the independent variables; laser power, scanning speed, hatch spacing and spot size) and the dependent variable (porosity).

Table 7: Analysis of variance model for porosity

	Sum of Squares	Degree of freedom	Mean square	F-value	p-value
Regression	16.8	4	4.2	4.9	0.019
Residual	8.5	10	0.853		
Total	25.3	14			

5.4.1.2 Analysis of correlations

According to Cohen (1988, pp. 79-81) multicollinearity exists when the independent variables are highly correlated (i.e. r = 0.50) and above. Cohen (1988, pp. 79-81) suggested the following guidelines in Table 8. Correlation analysis is used to describe the strength (magnitude) and direction of the linear relationship between two continuous variables. The direction between two continuous variables is indicated by either a positive or negative sign in front of the correlation coefficient.

Table 8: Limits for multicollinearity, as noted by Cohen (1988, pp. 79-81)

Correlation strength (magnitude)	Correlation coefficient
Small (Weak)	r = 0.10 - 0.29
Medium (Moderate)	r = 0.30 - 0.49
Large (Strong)	r = 0.50 - 1.0

The correlation values shown in Table 9 reflect the experimental design of process parameters used in Trial 1 and Trial 2.

Table 9: Pearson's correlation analysis (Cramer, 1988, pp. 139)

	Porosity	Laser power	Scanning speed	Hatch spacing	Spot size
Porosity	1	0.18	0.48	0.43	0.28
Power		1	0.07	0.36	0.91
Scanning Speed			1	-0.05	-0.12
Hatch Spacing				1	0.40
Spot Size					1

Note: Table 9 Pearson's correlation value r, demonstrating correlations**.** Strong correlations highlighted in blue; moderate correlation in yellow and weak correlations in grey

5.4.1.3 Tolerance & variance inflation factor

In a multiple linear regression analysis, the variance inflation factor (VIF) is used as an indicator of multicollinearity. The VIF is defined as the reciprocal of tolerance (1 /1- R^2) as it measures the combined effect of the dependency among the explanatory variables. Higher levels of VIF are known to adversely affect the results of a multiple regression analysis. The recommended acceptable levels of VIF, is a maximum value of 10 (Hair, 1995). VIFs set out in Table 10 were below the threshold of 10 indicating a low degree of multicollinearity.

Table 10: Tolerance & variance inflation factor values

	Tolerance	VIF
Power	0.139	7.206
Scanning Speed	0.793	1.261
Hatch Spacing	0.840	1.191
Spot Size	0.134	7.464

5.4.1.4 Normality

A probability plot is used as a general graphic technique to assess whether or not a data set follows a normal distribution (Chambers et al. 1983). The residuals appearing in the Normality Probability-Plot of the regression standardized residual should have a straight line-relationship with the predicted dependent variable (DV) scores. This would suggest no major deviations from normality. Figure 37, the porosity Normality P-P plot is indicative of the required straight line relationship, demonstrating no major deviation from normality.

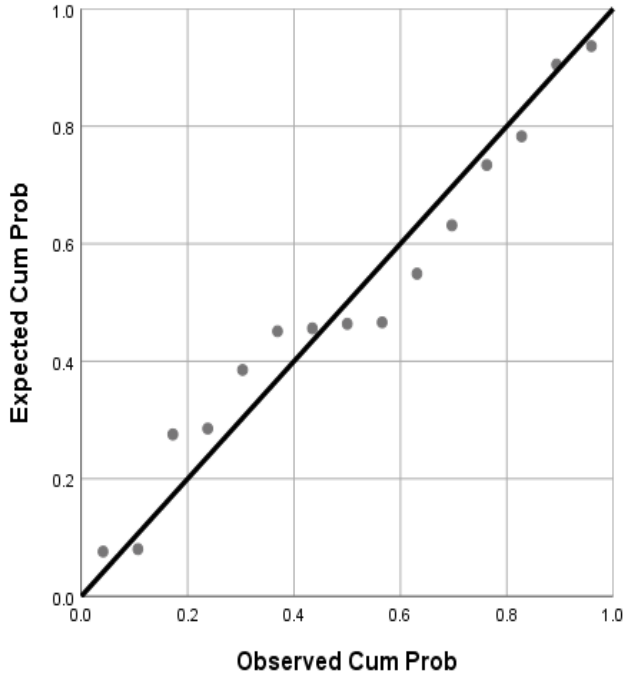

Figure 37: The P-P plot indicates that there is no measured major deviation from normality

5.4.1.5 Scatter plot

In linear regression, residual scatter plots provide a visual examination of the assumption of homoscedasticity between the predicted dependent variable scores and the errors of prediction. Homoscedasticity is defined as an assumption that means that the variance around the regression line is the same for all values of the predictor variable. Figure 38 indicates that the assumptions of homoscedasticity are not violated as all points are centered on 0.

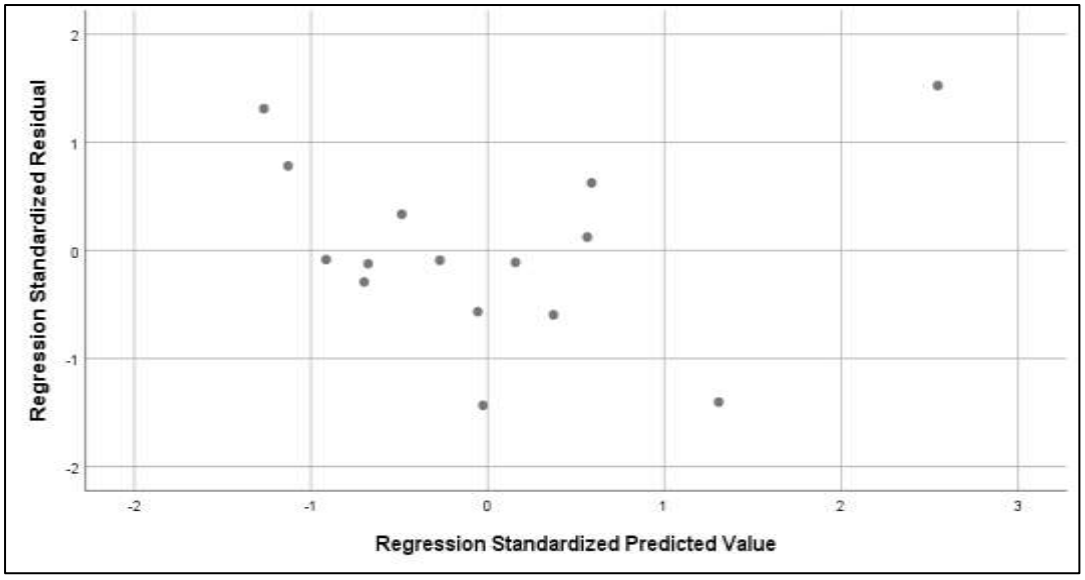

Figure 38: Scatter plot indicating homoscedasticity assumption is adhered to

5.4.1.6 Outliers

The outliers were checked by inspecting the Mahalanobis (MD) distances that were produced by the multiple regression program (Hadi, 1993). The maximum Mahalanobis distance is a statistical measure of the extent to which cases are multivariate outliers, based on a chi-square distribution assessed using $p < 0.0001$. The calculated maximum Mahalanobis distance value in this case is 8.1, compared to the critical value as according to chi-square independence degrees of freedom for a number of 4 independent values evaluated in this case, with the critical value of 18.5. Since the calculated maximum Mahalanobis distance is below the critical value there was no outliers.

5.4.1.7 Summary of multiple linear regression model for porosity

The main aim of performing a multiple regression model was to determine if the independent variables contribute in predicting the dependent variable. In this case, it was discovered that there was a statistically significant linear relationship between the dependent and independent variables. The strength and magnitude of the relationships was further determined through the analysis of collinearity statistics as set out in the correlations analysis tests Table 10. A second model was ran with variable (spot size) excluded, to test the model response upon exclusion of this factor. Table 12 sets out the reported coefficients of the independent variables, with corresponding p-values for laser power, a negative influence B coefficient of (-2.2) at p-value of 0.035 , scanning speed positive influence B coefficient (1.4) at p-value 0.005 , and spot size positive influence B coefficient of (0.0) at p-value 0.026. The p-value for all parameters except hatch spacing was below 0.05, indicating that variations in these parameters resulted in a significant variation in the amount of porosity.

The adjusted R^2 value incorporating the degree of freedom for the porosity multiple linear regression model (with spot size included) was 0.53, standard error of the estimate of 0.92, and an R^2 value of 0.664, implying that 66.4% variance of the dependent variable was explained by the independent variables.

Table 11: Unstandardized coefficients of the porosity model (including spot size)

	Unstandardized coefficients		T	p-value	95.0% Confidence interval for B	
	B	Std. error			Lower bound	Upper bound
	-6.622	2.019	-3.279	0.008	-11.121	-2.123
Power	-2.175	0.891	-2.44	0.035	-4.161	-0.189
Scanning speed	1.411	0.394	3.584	0.005	0.534	2.288
Hatch spacing	9.441	4.946	1.909	0.085	-1.579	20.461
Spot size	0.017	0.007	2.613	0.026	0.003	0.032

Table 12: Unstandardized coefficients of the porosity model (without spot size)

	Unstandardized coefficients		T	p-value	95.0% Confidence interval for B	
	B	Std. error			Lower bound	Upper bound
	-2.885	1.763	-1.636	0.130	-6.765	0.995
Power	-0.043	0.443	-0.096	0.925	-1.018	0.933
Scanning speed	0.954	0.436	2.187	0.051	-0.006	1.914
Hatch spacing	11.508	6.038	1.906	0.083	-1.782	24.799

Table 13: Comparison of the 2 linear regression models for porosity

	Model including spot size	Model without spot size
Constant	-6.620	-2.890
Sig (p-value)	0.008	0.130
Standardised coefficient (p-value);		
· **Power**	0.035	0.930
· **Scanning speed**	0.005	0.510
· **Hatch spacing**	0.085	0.083
· **Spot size**	0.026	
R square	0.664	0.430
Adjusted R square	0.530	0.280

Table 12 shows the coefficients for the linear regression model without spot size, whilst in Table 11 the spot size is included to indicate the level of significance of both cases. Table 13 compares the two models that were conducted (model with spot size and model without spot size). The model including spot size resulted in a p-value 0.008 whilst the model not including spot size resulted in a p-value 0.130. It was deduced that the model including spot size conforms to the maximum statistical standard level of significance, value of <0.05 since the p-value was 0.008. Excluding the spot size resulted in a multiple linear regression model with a p-value of 0.13, significantly higher than the cut-off value of 0.05. For the same model, the R-value was 0.43. For these reasons, the version of the multiple linear regression model that did not include spot size was not considered further.

Equation derived from the multiple linear regression model for porosity:

$$\boldsymbol{y = B_0 + B_1 x_1 + B_2 x_2 + B_3 x_3} \quad (7)$$

Porosity = - 6.6 - 2.2 (laser power, kW) + 1.4 (scan speed, m/s) + 9.4 (hatch spacing, mm)

According to the derived equation, the contribution of the various parameters, and of the constant, to the predicted porosity could be calculated. The calculations are summarized in Table 14**.**

Table 14: Coefficients and constants contribution to predicted porosity calculated from the linear regression model

Sample ID	Constant	Power	Scanning speed	Hatch spacing	Spot size	Predicted value (calc.)	Actual porosity (%)	Difference (calc.)
	-6.622	-2.175	1.411	9.441	0.017			
A1	-6.6	-2.2	4.2	1.2	4.3	0.9	0.9	0
A2	-6.6	-2.2	4.9	1.2	4.3	1.6	1.6	0
A3	-6.6	-2.2	5.6	1.2	4.3	2.3	1.8	0.5
A4	-6.6	-2.2	4.2	1.4	4.3	1.1	0.9	0.2
A5	-6.6	-2.2	4.9	1.4	4.3	1.8	1.4	0.4
A6	-6.6	-2.2	5.6	1.4	4.3	2.5	3.2	-0.7
A7	-6.6	-2.2	4.2	0.9	4.3	0.6	1.4	-0.8
A8	-6.6	-2.2	4.9	0.9	4.3	1.3	1.7	-0.4
A9	-6.6	-2.2	5.6	0.9	4.3	2	2	0
B1	-6.6	-4.4	5.6	2.3	7.7	4.6	6.2	-1.6
B2	-6.6	-4.4	2.8	2.3	7.7	1.8	0.6	1.2
B3	-6.6	-4.4	5.6	0.9	7.7	3.2	2.1	1.1
B4	-6.6	-4.4	2.8	0.9	7.7	0.4	1.8	-1.4
B5	-6.6	6.5	5.6	2.3	7.7	2.4	2.7	-0.3
B6	-6.6	-6.5	5.6	0.9	7.7	1.1	1.1	0

- Table 14 indicates the parameter contribution towards the predicted porosity per sample compared to the actual measured porosity. Samples manufactured at low laser power of 1 kW (A-series samples) indicated a small difference between predicted and actual measured porosity compared to the (B-series samples) manufactured at 2-3 kW, indicating that the multiple linear regression model was more accurate at lower levels of laser power.
- Porosity decreases with increase in energy density (due to high enough heat to melt the powder and allow adequate fusion) Figure 21.
- Porosity increases with increasing scanning speed, due to not enough time to allow adequate melting. Results presented in Figure 20 also indicated that higher scanning speed results in higher porosity.
- According to the empirical equation, the maximum laser power, scanning speed and hatch spacing that results in the lowest porosity is (2 kW laser power, 2 m/s scanning speed and 0.10 mm hatch spacing). The estimated porosity for this combination of processing parameters is 0.4%.

- Using the reported model coefficients and constants in the above equation, the actual porosity against the predicted porosity is shown in Figure 39. Figure 40 shows the difference between the actual and the predicted porosity against the predicted porosity. The fit of the model, as quantified by the R^2 value of 0.66 implies that 66% of the experimental data was predicted by the model. Collectively, the results in Figure 39 indicate the regression model to be acceptable, with the actual porosity about 1.05 times the predicted porosity, on average. The difference between the actual and the predicted porosity did not show any consistent trend - Figure 40.
- The maximum acceptable porosity is 0.2%. From Table 14, for sample B4 a porosity of 0.4% with sample process parameters (2 kW laser power, 2 m/s scanning speed, 0.10 mm hatch spacing and 450 µm spot size) was predicted. In contrast, the lowest actual porosity (0.6% was observed in sample B2, with process parameters of 2 kW laser power, 2 m/s scanning speed, 0.24 mm hatch spacing and 450 µm spot size. For sample B2, the predicted porosity was 1.8% (see Table 14). Clearly, the predictive capability of the multiple linear regression model was not adequate for levels of porosity below about 1%. The poor performance of the regression model at low levels of porosity could be due to a combination of the following:
    - The average porosity, for all samples, was 2.10%. The data set contained a significant number of samples with a high porosity.
    - The measurement of porosity was less reliable at a low level of porosity, as can be seen from the higher range in individual measurements of porosity at lower levels of porosity (Figure 19 discussed earlier in this chapter).

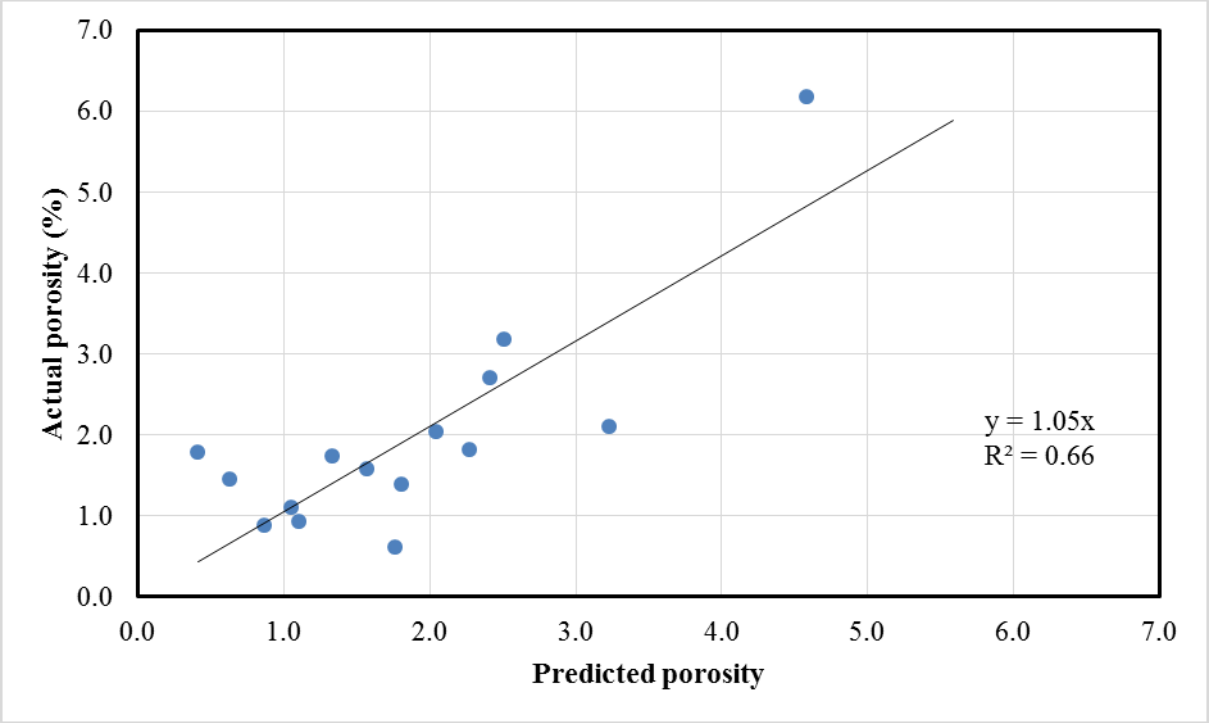

Figure 39: Cross plot of actual porosity vs. predicted porosity

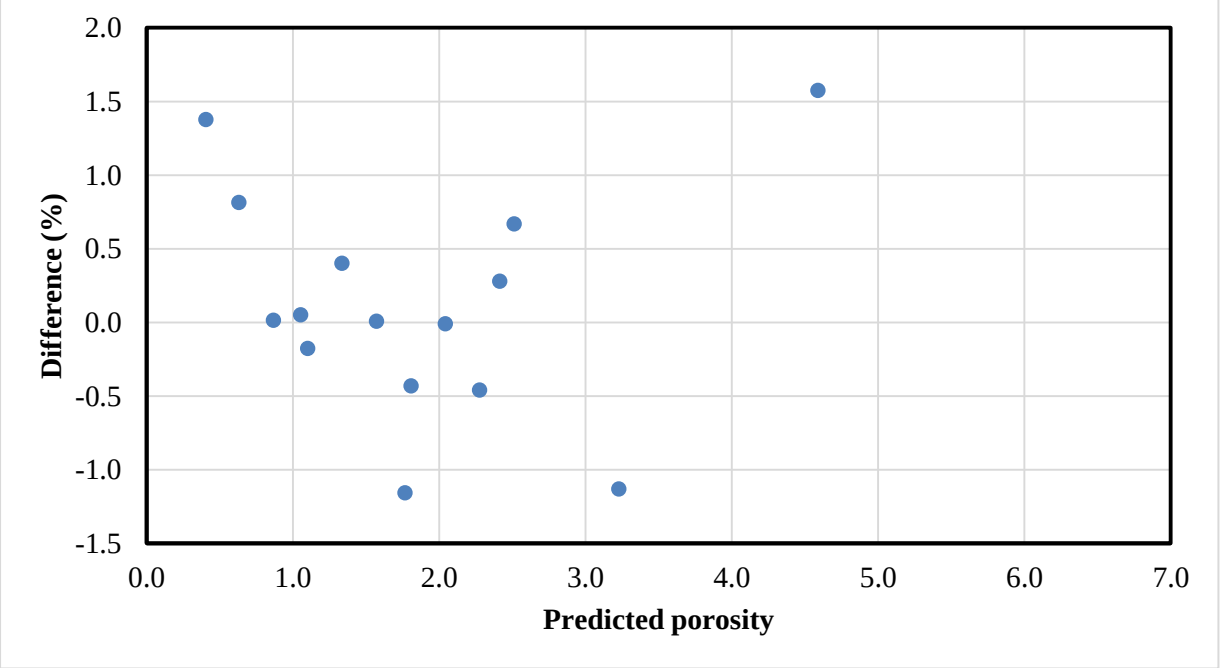

Figure 40: Difference between % actual porosity and predicted porosity, vs. predicted porosity

5.4.2 Evaluation of the effect of process parameters on hardness (average hardness along the build)

Table 15: Analysis of variance model for hardness

	Sum of squares	Degree of freedom	Mean square	F-value	p-value
Regression	11911	4	2978	0.148	0.96
Residual	201106	10	20111		
Total	213017	14			

The reported p-value of the multiple linear regression model for hardness was 0.96, Table 15. The average hardness along the build of each sample in Table 18 & 19 in the appendix was used to derive the model. As the p-value was well above 0.05, it indicated that there is no statistical linear relationship between the set of independent variables and hardness (Fisher, 1973). The poor prediction capability of the multiple linear regression model was consistent with the small variation in hardness (Figure 31 to 36, in section 4.5).

6. CONCLUSIONS

The following conclusions were made:

- The microstructural constituents i.e. (alpha and columnar prior beta grain size, and α martensite phase) was found to be significantly influenced by the change in process parameters , however the hardness did not have a considerable variation in range. It can then be concluded that the microstructure is dependent on the process variables, where-as hardness dependency is limited.
- The technique used to determine the sample porosity, using density measurements, was reliable at porosity levels above about 2%, but was less reliable at lower levels of porosity.
- Porosity is a function of laser power, scanning speed, hatch spacing and energy density.
- The extent of the influence of spot size could not be quantified in the used set of parameters.
- Linear relationships were developed to predict porosity of Ti6Al4V under the set of parameters used. The resultant equation was as follows;

Porosity = - 6.6 - 2.2 (laser power, kW) + 1.4 (scan speed, m/s) + 9.4 (hatch spacing, mm) + 0.017(spot size, μm).

Subject to the following limitations:

laser power: 1 to 3 kW;

scan speed: 2 to 4 m/s;

hatch spacing: 0.10 to 0.24 mm;

Spot size: 250 or 450 μm.

Porosity > 1%

- A decrease in laser power was found to have a negative influence on porosity. A too high laser power induces micro porosity. An increase in scanning speed and hatch spacing increases the likelihood of porosity.
- Insufficient energy density resulted in increased fraction porosity, medium energy density decreased porosity, whilst too high energy densities resulted in decreased fraction porosity and introduction of small micro round pores.
- It must be noted that too high power and too high scanning speed does not guarantee a porosity free product.

7. RECOMMENDATIONS

Based on the conclusions made in the current study the following recommendations are made:

- Process variables should be designed to allow enough time for powder melting, smaller hatch distances for adequate melt pool fusion, and just enough laser power to provide enough energy to enhance adequate powder melting, e.g. the following process parameter combination at spot size 250 and 450 µm achieved the least porosity:
  - At 250 µm spot size, 1 kW laser power, 3 m/s lowest scanning speed and 0.13 mm hatch spacing, the lowest porosity attained was 0.88%.
  - At 450 µm spot size, 2 kW laser power, 2 m/s lowest scanning speed, 0.24 mm hatch spacing, the lowest porosity attained was 0.61%.

- Future research work using other techniques aimed determining porosity in the range smaller that 2%, techniques such as X-ray computed tomography scanning.

8. REFERENCES

Antonysamy, AA 2012, Microstructure, Texture and Mechanical Property Evolution during Additive Manufacturing of Ti6Al4V Alloy for Aerospace Application, Doctoral Thesis, University of Manchester: School Of Materials, viewed 22 May 2017, https://www.escholar.manchester.ac.uk/uk-ac-man-scw:160535.

Attar, H, Bonisch, M, Calin, M, Zhang, LC, Scudino, S, & Eckert, J 2014, 'Selective laser melting of in situ titanium-titanium boride composites: Processing microstructure and mechanical properties' Acta Materia, Volume 76, pp. 13-22.

ASTM B822-17, 2017. Standard Test Method for Particle Size Distribution of Metal Powders and Related Compounds by Light Scattering, , West Conshohocken, ASTM International PA, http://www.astm.org

ASTMISO/ASTM52900-15, 2015. Standard Terminology for Additive Manufacturing-General Principles-Terminology, West Conshohocken: ASTM International, PA, https://doi.org/10/1520/ISOASTM52900-15.

Bauereib, A, Scharowsky, T & Korner, C 2014, 'Defect generation and propagation mechanism during additive manufacturing by selective beam melting', J. Material Processing Technology, Volume . 214, pp. 2522-2528.

Bourell, D, Coholic, J, Chalancon, A & Bhat, A 2017, 'Evaluation of Energy Density Measures and Validation for Powder Bed Fusion of Polyamide', CIRP Ann. Manufacturing Technology, Volume 66 (1), pp. 217-220.

Chambers, J, Cleveland, W, Kleiner, B & Tukey, P 1983, Graphical Methods for Data Analysis, Wadsworth, Bellmont

Chow, M, Bordat Chec, E & Knopf, G 2013, 'Experimental study on the effect of varying focal offset distance on laser micro-polished surfaces', The International Journal of Advanced Manufacturing Technology, Volume 67(9-12), pp. 2607-2617.

Cohen, J 1988, Statistical Power Analysis for the Behavioural Sciences, New York University, 2nd Edition, pp.79-81

Cramer, D 1998, 'Fundamental Statistics for Social Research', London, Routledge, Volume 39 (7), pp.1035

Donachie, MJ 2000, 'Understanding the metallurgy of titanium: A Technical Guide', Materials Park, Ohio: ASM International, pp. 13-21.

Easton, MA, Qian, M, Prasad, A & StJohn, DH 2016, 'Recent advances in grain refinement of light metals and alloys', Current Opinion in Solid State and Materials Science Elsevier, Volume 20 (1), pp. 13-24 http://dx.doi.org/10.1016/j.cossms.2015.10.001.

EEF, The Manufactures Organization 2016, The 4th Industrial Revolution: A Primer For Manufactures, Ref: 16.11.POL.CR.NB https://www.makeuk.org/insights/publications.

Fabbro, R. (2019), "Scaling laws for the laser welding process in keyhole mode", Journal of Materials Processing Technology, Vol. 264, pp. 346–351.

Fisher, R 1973, Statistical Methods and Scientific Inference, 3rd Edition Ed, Collins Macmillan, https://www.amazon.com/Statistical-Methods-Scientific-Inference-Third/dp/B001NFM5YA

Frazier, W 2014, 'Metal Additive Manufacturing', A Review. ASM International, Volume 23(6), pp. 1917-1928.

Galarraga, H, Lados, DA, Dehoff,R R, Kirka,M M & Nandwna, P 2016, 'Effects of the microstructure and porosity on properties of Ti6Al4V ELI alloy fabricated by electron beam melting (EBM)', Additive Manufacturing Elsevier, Volume 10, pp. 47-57.

Gong, H, Rafi, K, Starr, T & Stucker, B 2013, 'The Effects of Processing Parameters on Defect Regularity in Ti6Al4V Parts Fabricated By Selective Laser Melting and Electron Beam Melting' Department of Industrial Engineering, Department of Chemical Engineering, J.B School of Engineering, University of Louisville, Louisville, KY40292, pp. 424-439.

Hadi, A, Simonoff, J 1993, 'Procedures for the identification of multiple outliers in linear models', Journal of the American Statistical Association, Volume 88, pp. 1264-1272.

Hair, J, Anderson, RE, Tatham, RL, Black, WC 1995, 'Multivariate Data Analysis (3rd Edition)' New York: Macmillan.

Hutchinson, B 2015, 'Critical Assessment 16: Anisotropy in Metals', Material Science and Technology, Volume 31(12), pp. 1393-1401.

Kamath, C, EL-Dasher, B, Gallegos, WE, King, GF & Sisto, A 2014, 'Density of Additively Manufactured 316l SS Parts Using Laser Powder-Bed Fusion at Powers up to 400W', Int. J. Adv. Manufacturing. Technology, pp. 65-78.

Kasperovich, G, Haubrich, J, Gussone, J & Requena, G 2016, 'Correlation between porosity and processing parameters in Ti6Al4V produced by selective laser melting', Materials and Design, Institute of Materials Research, German Aerospace Centre (DLR), Germany, Volume 105, pp. 160-170.

King, WE, Barth, HD, Castillo, VM, Gallegos, GF & Gibbs, JW 2014, 'Observation of keyhole-mode laser melting in laser powder-bed fusion additive manufacturing', J. Materials Processing Technology, Volume 214, pp. 2915-2925.

Kobryn, P A & Semiatin, SL 2001, 'The Laser Additive Manufacture of Ti6Al4V', JOM, Volume 53 (9), pp. 40-42.

Koike, M, Guo. ML, Chahine, G, Kovacevic, T, & Okabe, T 2011, 'Evaluation of titanium alloy fabricated using electron beam melting for dental applications', Material Processing Technology, Volume 211, pp. 1400-1408.

Kumar, S, & Pityana, S 2010, 'Laser-Based Manufacturing of Metals', Algeria, 2nd International Conference of Laser and Plasma Applications in Material Science.

Kurz, W, Bezencon, C & Gaumann, M 2001, 'Columnar to equiaxed transition in solidification processing', Science and Technology Advance Materials, Volume 2, pp. 185-191.

Lampman, S 1990, 'Properties and selection: Nonferrous alloys and special-purpose materials: Wrought titanium and titanium alloys', ASM International, Volume 2 (10), pp. 592-633.

Liu, B, Wildman, R, Tuck, C, Ashcroft, I & Hague, R 2011, 'Investigation of the effect of particle size distribution on processing parameter optimisation in selective laser melting process', Additive Manufacturing Research Group, Loughborough University, pp. 227-238.

Louw, D, 2016, Maximising the build rate for laser powder bed fusion of Ti6Al4V with a 3kW laser, University of Pretoria: Faculty of Engineering, the Built Environment and Information Technology.

Mani, M, Lane, B, Donmez, A, Feng, S, Moylan, S & Fersperman, R 2015, 'Measurement Needs for Real-Time Control of Additive Manufacturing Powder Bed Fusion Processes', National Institute of Standards and Technology, Volume 8036, pp. 1-46.

Mumtaz, KA & Hopkinson, N 2010, 'Selective laser melting of thin wall parts using pulse shaping' Materials Processing Technology, Volume 210, pp. 279-287.

Mower, T & Long, M 2016, 'Mechanical behaviour of additive manufactured, powder-bed laser-fused materials', Materials Science & Engineering A, Volume A651, pp. 198-213.

Murr, L, Esquivel, E, Quinones, S, Gaytan, S, Lopez, M & Martinez, E 2009, 'Microstructure and mechanical properties of electron beam rapid manufactured Ti-6Al-4V biomedical prototypes compared to wrought Ti-6Al-4V', Material Characterisation, Volume 119, pp. 494-528.

Tolochko, NK, Mozzharov, S, Yardriotsev, Laoui, L & Froyen, V 2004, 'Balling process during selective laser treatment of powders', Rapid Prototype, Volume 10 (2), pp. 78-87.

Pang, S, Chen, W, Wang, W 2014, 'A quantitative model of keyhole instability induced porosity in laser welding of titanium alloy', Metallurgy Materials Trans, Volume 45A (A), pp. 2808-2018.

Pederson, R 2002, 'Microstructure and Phase Transformation of Ti6Al4V', Lulea University of Technology, Department of Applied Physics and Mechanical Engineering, Division of Engineering Materials.

Pinkerton, A J, Karadge, M, Syed, WUH, & Li, L 2006, 'Thermal and microstructural aspects of laser direct metal deposition of Waspaloy', J Laser Applications, Volume 18, pp. 216-226.

Rai, R, Palmer, TA, Elmer, JW, & Derbroy, T 2009, 'Heat transfer and fluid during electron beam welding of 304 L stainless steel alloy', Applied Physics, Volume 88, pp. 54-61.

Sames, WJ, List, FA, Pannala, S, Dehoff, RR & Babu, SS 2016, 'The metallurgy and processing science of metal additive manufacturing', International Materials Reviews, pp. 1743-2804.

Shukla, M, & Verma, V 2014, 'Finite Element Simulation and Analysis of Laser Metal Deposition', Cape Town 6th International Conference on Mechanical Production & Automibile Engineering.

Tang, M, Pistorius, PC & Beuth, J 2017, 'Prediction of lack-of-fusion porosity for powder bed fusion', Additive Manufacturing, pp. 39-48.

Tang, M, Pistorius, PC, Montgomery & Beuth, J 2018, 'Build Rate Optimisation for Powder Bed Fusion', ASM International, pp. 641-647.

Technologies, P, 2006-2017. Metallographic Specimen Etching: Metallographic Etchants. [Online]

Available at: http://www.metallographic.com/Etchants/Etchants.htm, [Accessed 21 March 2018].

Thijs, L, Verhaeghe, F, Craeghs, T, Van Humbeeck, J & Kruth, JP 2010, 'A study of the microstructural evolution during selective laser melting', Acta Materialia, Volume 58, pp. 3303-3312.

Vilaro, T, Colin, C & Bartout, JD 2011, 'As fabricated and heat-treated microstructures of Ti6Al4V alloy processed by SLM', The Minerals, Metals & Materials Society and ASM International, Volume 42A, pp. 3190-3199.

Vrancken B, Van Humbeeck, J, Thijs, L 2012, 'Heat treatment of Ti6Al4V produced by Selective Laser Melting: Microstructure and Mechanical Properties', Journal of Alloys and Compounds, Volume 541(0), pp. 177-185.

Wang, T, Zhu, YY, Zhang, SQ, Tang, HB, Wang, HM 2015, 'Grain morphology evolution behaviour of titanium alloy components during laser melting deposition additive manufacturing', Journal of Alloys and Compounds, Volume 632, pp. 505-513.

Wanhill, R, & Barter, S 2012, 'Fatigue of Beta Processed and Beta Heat Treated Titanium Alloys', Springer Briefs in Applied Science and Technology, Issue DOI: 10.1007/978-94-007-2524-9_2.

Wong, KV, & Hernandez, A 2012, 'A review of Additive Manufacturing', International Scholarly Research Network, ISRN Mechanical Engineering, Volume 2012, Article ID 208760, pp.10

Wu, X, Liang, J, Mei, J, Mitchell, C, Goodwin & PS, Voice, W 2004, 'Microstructures of laser-deposited Ti6Al4V', Material Design, Volume 25, pp. 137-144.

Xu, W, Sun, S, Elambasseril, J, Liu, Q, & Qian, M 2015, 'Ti6Al4V Additively Manufactured by Selective Laser Melting with Superior Mechanical Properties', JOM, The Minerals, Metals & Materials Society, Volume 67(3), pp. 668-673.

Zhang, H, Zhu, H, Qi, T, Hu, Z, & Zheng, X 2016, 'Selective laser melting of high strength Al-Cu-Mg: Processing, microstructure and mechanical properties', Materials Science & Engineering A, Volume A656, pp. 47-54.

9. APPENDIX

9.1 Porosity results

Table 16: Individual density measurements of all samples

Sample no.	Density (g/cm^3)	Average density (g/cm^3)	%Density	Porosity	Average porosity	Range in porosity	Range/average porosity
A1	4.3842	4.389	98.97	1.03	0.93	0.20	0.21
	4.3929		99.16	0.84			
	4.3913		99.13	0.87			
A2	4.3665	4.365	98.57	1.43	1.47	0.13	0.09
	4.3667		98.57	1.43			
	4.3610		98.44	1.56			
A3	4.3481	4.349	98.15	1.85	1.83	0.05	0.03
	4.3504		98.20	1.80			
	4.3496		98.19	1.81			
A4	4.3868	4.388	99.02	0.98	0.95	0.21	0.22
	4.3845		98.97	1.03			
	4.3936		99.18	0.82			
A5	4.3656	4.369	98.55	1.45	1.38	0.25	0.18
	4.3655		98.54	1.46			
	4.3764		98.79	1.21			
A6	4.2852	4.287	96.73	3.27	3.23	0.33	0.10
	4.2813		96.64	3.36			
	4.2958		96.97	3.03			
A7	4.3663	4.366	98.56	1.44	1.44	0.02	0.02
	4.3652		98.54	1.46			
	4.3662		98.56	1.44			
A8	4.3443	4.353	98.07	1.93	1.74	0.31	0.18
	4.3581		98.38	1.62			
	4.3571		98.35	1.65			
A9	4.3412	4.344	98.00	2.00	1.94	0.25	0.13
	4.3401		97.97	2.03			
	4.3511		98.22	1.78			
B1	4.3081	4.311	97.25	2.75	2.69	0.11	0.04
	4.3110		97.31	2.69			
	4.3130		97.36	2.64			
B2	4.3369	4.337	97.90	2.10	2.10	0.07	0.03
	4.3389		97.94	2.06			
	4.3357		97.87	2.13			
B3	4.1556	4.157	93.81	6.19	6.16	0.04	0.01

	4.1568		93.83	6.17			
	4.1575		93.85	6.15			
B4	4.3481	4.351	98.15	1.85	1.78	0.14	0.08
	4.3519		98.24	1.76			
	4.3541		98.29	1.71			
B5	4.4001	4.403	99.33	0.67	0.61	0.13	0.22
	4.4060		99.46	0.54			
	4.4039		99.41	0.59			
B6	4.3881	4.381	99.05	0.95	1.11	0.32	0.29
	4.3819		98.91	1.09			
	4.3741		98.74	1.26			

9.2 Beta grain size

Table 17: Average beta grain size length (µm)

Columnar grains size dimension across the width (µm)										
Sample No.	**Laser power (kW)**	**Energy density (J/mm^3)**	**No. of grains measured**							
			1	**2**	**3**	**4**	**5**	**6**	**Average**	**Stand dev.**
A1	1	51	57	88	51	129	58	95	80	28
A2	1	44	137	282	275	231	92	59	179	88
A3	1	38	65	45	35	55	117	116	72	33
A4	1	44	116	44	86	49	85	134	86	32
A5	1	38	67	201	136	178	368	130	180	94
A6	1	33	88	58	202	255	200	145	158	69
A7	1	67	116	120	75	86	55	45	83	28
A8	1	57	190	183	201	383	115	110	197	91
A9	1	50	48	55	97	100	58	80	73	21
B1	2	42	28	91	17	72	30	64	50	27
B2	2	83	352	301	111	233	270	211	246	76
B3	2	100	118	65	105	87	51	62	81	24
B4	2	200	157	110	122	164	85	95	122	30
B5	3	62	157	62	147	90	143	70	112	39
B6	3	150	394	191	166	355	80	55	207	128

9.3 Hardness results

Table 18: Trial 1 hardness results (1 kW low laser power)

Force:	300 (g)								
Dwell time :	10 (sec)								
Calibration:	0.10627 (µm/pixel)								
Magnification:	40x								
Hardness longitudinal									
Position (µm)	Sample A1	Sample A2	Sample A3	Sample A4	Sample A5	Sample A6	Sample A7	Sample A8	Sample A9
0	382	389	384	380	374	365	383	374	363
2000	382	388	372	377	376	365	377	374	360
3000	376	382	367	369	372	361	377	369	350
4000	376	382	366	368	369	354	375	375	358
5000	375	380	365	367	367	354	366	376	353
6000	374	380	363	364	367	354	365	375	353
7000	374	374	363	364	364	350	363	377	358
8000	374	373	363	363	362	346	359	353	357
9000	373	371	361	361	361	346	364	369	343
10000	372	368	359	361	359	346	357	365	353
Average	376	379	366	367	367	354	369	371	355
Stand dev	3	7	7	6	5	7	8	7	5

Table 19: Trial 2 Hardness results (2-3 kW high laser power)

Force:	300 (g)					
Dwell time :	10 (sec)					
Calibration:	0.10627 (µm/pixel)					
Magnification:	40x					
Hardness longitudinal						
Position (µm)	Sample B1	Sample B2	Sample B3	Sample B4	Sample B5	Sample B6
0	357	418	354	355	399	354
2000	357	413	356	357	399	346
3000	346	369	346	346	345	339
4000	337	354	337	337	340	343
5000	337	343	337	337	338	325
6000	336	373	336	336	333	339
7000	336	336	336	336	330	316
8000	334	339	334	334	320	312
9000	352	350	332	352	321	325
10000	332	329	332	332	320	316
Average	345	340	342	342	362	332
Stand dev	28	8	9	9	30	14

Table 20: Analysis of variance model for hardness

	Sum of squares	Df	Mean square	F	p-value
Regression	11911	4	2978	0.15	0.960b
Residual	201106	10	20111		
Total	213017	14			

Table 21: Pearson's correlation analysis for hardness

	Average hardness	Power	Scanning speed	Hatch spacing	Spot size
Average Hardness	1	0.2	-0.06	0.11	0.23
		1	0.073	0.364	0.91
			1	-0.048	-0.12
				1	0.4
					1

Table 22: Standardized and unstandardized coefficients of the hardness model

	Unstandardized coefficients		Standardized coefficients	T	p-value	95.0% Confidence interval for B		Collinearity statistics	
	B	Std. error	Beta			Lower bound	Upper bound	Tolerance	VIF
Constant	220	310		0.71	0.49	-470	911		
Power	-4.18	137	-0.03	-0.03	0.98	-309	301	0.14	7.21
Scanning speed	-4.9	60	-0.03	-0.08	0.94	-140	130	0.79	1.26
Hatch spacing	42	760	0.02	0.06	0.96	-1650	1734	0.84	1.19
Spot size	0.3	1	0.25	0.29	0.78	-2	2.6	0.13	7.46

9.4 Porosity linear regression model (without spot size)

Table 23: Standardized and unstandardized coefficients of the porosity model (without spot size)

	Unstandardized coefficients		Standardized coefficients	T	p-value	95.0% Confidence interval for B		Collinearity statistics	
	B	Std. error	Beta			Lower bound	Upper bound	Tolerance	VIF
Constant	-2.88	1.76		-1.64	0.13	-6.76	1		
Power	-0.04	0.44	-0.02	-0.1	0.92	-1.02	0.93	0.86	1.16
Scanning Speed	0.95	0.44	0.5	2.19	0.05	-0.01	1.91	0.99	1.01
Hatch Spacing	12	6.04	0.47	1.91	0.08	-1.78	24.8	0.86	1.16